Meteorological Drivers of North American Monsoon Extreme Precipitation Events

Shiheng Duan[1], Paul Ullrich[2], and William R. Boos[3]

[1]University of California, Davis
[2]University of California Davis
[3]University of California, Berkeley

December 7, 2022

Abstract

In this paper the meteorological drivers of North American Monsoon (NAM) extreme precipitation events (EPEs) are identified and analyzed. First, the NAM area and its subregions are distinguished using self-organizing maps (SOM) applied to the Climate Prediction Center (CPC) global precipitation dataset. This delineation emphasizes the distinct extreme precipitation character and drivers in each subregion, and we subsequently argue these subregions are more suitable for regional analysis given the inhomogeneous geographical features in the NAM area. For each EPE, defined as daily precipitation exceeding the 95th precipitation percentile, five synoptic features and one mesoscale feature are investigated and assigned as potential drivers. Essentially all EPEs can be associated with at least one selected driver, with only one event remaining as unclassified. The attribution result demonstrates the dominant role of Gulf of California moisture surges, followed by mesoscale convective systems. Finally, a frequency and probability analysis is conducted to contrast precipitation distributions conditioned on the associated meteorological drivers. Interactions and influences among candidate features are revealed by the precipitation probability density functions.

Meteorological Drivers of North American Monsoon Extreme Precipitation Events

Shiheng Duan[1], Paul Ullrich[1], William Boos[2]

[1]Atmospheric Science Graduate Group, University of California, Davis
[2]Department of Earth and Planetary Science, University of California, Berkeley

Key Points:

- Seven subregions of the North American Monsoon with distinct precipitation character are identified
- Almost all subregional extreme precipitation events are associated with at least one atmospheric feature
- Co-occurrence of meteorological features may or may not drive increases in precipitation

Corresponding author: Shiheng Duan, `shiduan@ucdavis.edu`

Abstract

In this paper the meteorological drivers of North American Monsoon (NAM) extreme precipitation events (EPEs) are identified and analyzed. First, the NAM area and its subregions are distinguished using self-organizing maps (SOM) applied to the Climate Prediction Center (CPC) global precipitation dataset. This delineation emphasizes the distinct extreme precipitation character and drivers in each subregion, and we subsequently argue these subregions are more suitable for regional analysis given the inhomogeneous geographical features in the NAM area. For each EPE, defined as daily precipitation exceeding the 95th precipitation percentile, five synoptic features and one mesoscale feature are investigated and assigned as potential drivers. Essentially all EPEs can be associated with at least one selected driver, with only one event remaining as unclassified. The attribution result demonstrates the dominant role of Gulf of California moisture surges, followed by mesoscale convective systems. Finally, a frequency and probability analysis is conducted to contrast precipitation distributions conditioned on the associated meteorological drivers. Interactions and influences among candidate features are revealed by the precipitation probability density functions.

Plain Language Summary

Extreme precipitation is of great importance for both scientific research and socioeconomic activities. The North American Monsoon region and its subregions, which are extracted from a precipitation dataset, are the main subjects of this study. The extreme precipitation events in each subregion are associated with at least one candidate atmospheric driver, and the result demonstrates distinct major precipitation drivers among subregions. Furthermore, depending on the subregions and drivers, the precipitation rate may increase or decrease when two candidate factors co-occur, where several double drivers combinations are examined.

1 Introduction

Monsoons are continental-scale circulation systems that develop in response to seasonal changes in the contrast in energy sources between continents and adjacent oceanic regions (Vera et al., 2006; Geen et al., 2020). They are known for driving substantial regional precipitation, and are critical to the Earth's hydroclimate system. In this study, we focus on the North American Monsoon (NAM) and examine the meteorological environments and feature drivers of both precipitation and extreme precipitation when the NAM is active. We show that essentially all extreme precipitation events (EPEs) can be linked to one or more meteorological features. This feature-based decomposition is subsequently employed to draw novel insights into the drivers of precipitation in the NAM and its subregions.

The first challenge in characterizing precipitation in the NAM is to actually delineate the NAM region. Ramage (1971) used the reversal in the large-scale lower tropospheric circulation to identify the monsoon domain. This approach has been applied widely to define several monsoon indices, such as the Webster-Yang monsoon index for the South Asian monsoon, the Australian monsoon index, the South Asian monsoon index and the dynamic Indian monsoon index (Webster & Yang, 1992; Hung & Yanai, 2004; Goswami et al., 1999; B. Wang & Fan, 1999). However, this circulation-based method is not suitable for the NAM region, since the NAM does not exhibit the same sort of domain-wide seasonal zonal wind reversal that characterizes monsoons in other regions (de Carvalho & Jones, 2016). Precipitation has also been used to identify monsoonal regions: for instance, Liu et al. (2016) define global monsoon systems using the climatological precipitation difference between MJJAS (May-September) and NDJFM (November-March). If defined in terms of precipitation seasonal variability, the NAM region refers to the region roughly bounded to the south by Central America and stretching into the south-

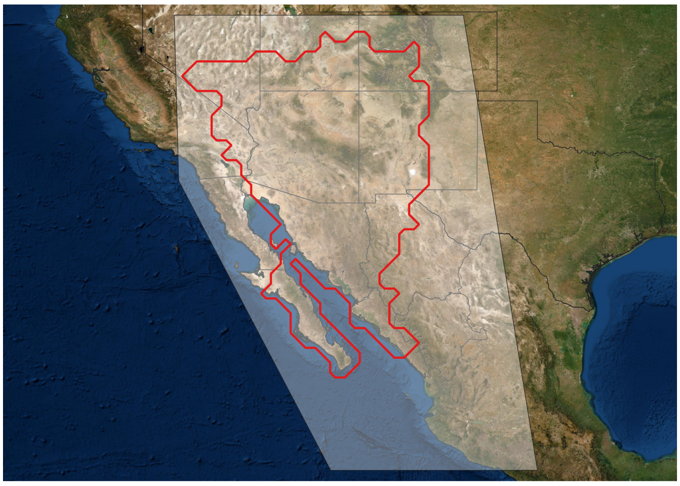

Figure 1. The NAM regional domain. The white contour is from the North American Monsoon Experiment Forecast Forum. The red contour denotes the domain identified from the ensemble SOMs in this study.

western US (Lee & Wang, 2014; Mohtadi et al., 2016; Liu et al., 2016; B. Wang et al., 2018). The NAM Experiment (NAME) (W. Higgins et al., 2006) offers another definition of the NAM region, which roughly encompasses the southwestern United States and northwestern Mexico (Figure 1). This region is much smaller and offset to the north from the NAM region that emerges from precipitation seasonal variability.

Despite being termed as the "NAM region" in the NAME, the regular trapezoid bounded by straight lines in latitude-longitude space is not treated as an exact boundary. Indeed, the term "NAM region" has been used to refer to a rectangular latitude-longitude box, or to specific states such as Arizona or New Mexico; this has especially been the case in climate change studies focused on long-term climatological precipitation signals (Douglas & Englehart, 2007; Finch & Johnson, 2010a; Cook & Seager, 2013; Varuolo-Clarke et al., 2019). Although these choices can simplify computations, such approximations are not appropriate for regional precipitation studies. Such structured regions cover areas with distinct precipitation mechanisms and drivers. This is especially true in the vicinity of the NAM, where the complex terrain leads to precipitation being shaped by the mechanical influence of orography on winds, together with local thermodynamic conditions (Boos & Pascale, 2021). As such, we argue that a delineation of the NAM region emphasizing localized precipitation features should be used for studies focused on NAM precipitation. The "NAM region" identified in this manner, along with its subregions which we will discuss later, is necessary to establish a foundation for the precipitation and extreme precipitation analysis pursued in this study.

EPEs, which occur when the precipitation rate is in the long tail of its distribution, are of considerable importance for scientific research, socioeconomic impacts, and water management considerations. EPEs are generally defined as events in which the precipitation rate exceeds a certain threshold, typically using one of two methods: parametric or non-parametric (Anagnostopoulou & Tolika, 2012). Parametric approaches include peaks-over-threshold (POT) and block maxima (Barlow et al., 2019). The POT method sets an initial threshold and fits the data with a generalized Pareto distribution (Acero et al., 2011), while the block maxima method focuses on the series of maximum values from a regular interval (such as maximum daily precipitation in each month), and fits the maximum data series with a generalized extreme value distribution (Alaya et al., 2020). The non-parametric approach does not make assumptions about the probability distribution of the data, and is often used with percentiles, such as the 95th percentile precipitation amount of rainy days (pq95) and the 99th percentile precipitation amount of rainy days (pq99) (Kunkel et al., 2012; Agel et al., 2018; Myhre et al., 2019). In this study, we adopt the non-parametric approach and define the threshold for EPEs from pq95.

To understand the meteorological causes of EPEs, Barlow et al. (2019) reviewed a set of potential meteorological systems for extreme precipitation over North America, such as tropical cyclones, mesoscale convective systems, frontal systems, and atmospheric rivers. Specifically for the NAM region, Kunkel et al. (2012) demonstrated the important role played by frontal systems in summertime, and Sierks et al. (2020) revealed the connection between upper-level wave breaking and EPEs in the Lake Mead watershed. These studies provide candidate meteorological systems to comprehensively understand the drivers of NAM precipitation.

In this study, we first identify the NAM domain and its subregions from a gridded precipitation dataset, delineating regions using local precipitation characteristics. The drivers of precipitation and EPEs in these regions are subsequently investigated using feature tracking and attribution. Section 2 describes the precipitation and reanalysis datasets in this study. Precipitation-based NAM domain and subdomain demarcation is described in Section 3. Section 4 introduces the candidate drivers of the NAM EPEs, as well as the corresponding detection methods and datasets, then examines the distribution of precipitation related to each driver.

2 Data

In this study, precipitation data from the Climate Prediction Center (CPC) Global Unified Gauge-Based Analysis of Daily Precipitation (referenced to as the CPC dataset) is used. CPC data is based on gauge observations and provides daily precipitation analysis globally at 0.5 degree grid spacing from January 1st 1979 to present (Xie et al., 2010). Consistent with prior research on the NAM, we extract precipitation from a candidate domain consisting of the contiguous US (CONUS) and Mexico. Since the CPC dataset relies on gauge observations, the specific time period that defines a day varies across the globe. For CONUS and Mexico, they share the same time window: from 1200 to 1200 UTC. Meteorological conditions are derived from the ERA5 reanalysis dataset. This product provides hourly reanalysis atmospheric fields with a 30-km horizontal resolution (Hersbach et al., 2020). The record spans from 1950 to present, although we subset the period 1979 to 2018 to coincide with the precipitation data coverage. Additionally, when the hourly data is averaged to derive daily records, the time window is set to 12Z-12Z to keep accord with the CPC precipitation time interval.

3 Identification of NAM Subregions

3.1 Self Organizing Maps

Self organizing maps (SOMs) is an unsupervised machine learning method that takes high-dimensional data as input and creates spatially organized internal representations of input vectors (Kohonen & Honkela, 2007). Details on the training process can be found in Kohonen and Honkela (2007). After the SOMs has converged, each sample is assigned to a node, which can be viewed as the cluster label.

SOMs has been applied in previous studies for pattern recognition. For example, Agel et al. (2018) used SOMs with tropopause pressure anomalies to find the large-scale patterns associated with extreme precipitation. In this work we follow Swenson and Grotjahn (2019), who used SOMs to classify different precipitation regimes over the CONUS. Before applying SOMs, we first take the cube root of precipitation as in Stidd (1953) to transform it from a highly skewed distribution to an approximately normal distribution.

Then the long-term daily mean (LTDM) is calculated, excluding leap days. The LTDM is normalized to the range from 0 to 1 before training the SOMs according to

$$\text{LTDM}_{\text{normalized}} = \frac{\text{LTDM} - \min(\text{LTDM})}{\max(\text{LTDM}) - \min(\text{LTDM})}. \tag{1}$$

This preprocessing informs us of the occurrence of extreme precipitation normalized within each grid cell, rather than the absolute precipitation amount.

The number of output nodes (i.e., the number of clusters) is prescribed before training SOMs. Since there is no prior knowledge of the correct number of clusters, to avoid arbitrariness and ensure robustness, an ensemble method is employed with the number of nodes ranging from 10 to 20. The final NAM region is then based on the intersection of all the ensemble.

3.2 NAM Domain and Subregions

As demonstrated previously, the long-term daily mean precipitation (January to December), preprocessed by equation 1, is used as the input to the SOMs. The NAM domain derived from the ensemble SOMs shares similar location but smaller extent compared with the NAME as shown in Figure 1. The individual SOMs ensemble results are depicted in Figure S1. Although the cluster boundaries vary with the number of clusters, the general locations and patterns are consistent among all the SOMs results. It should be noted that the SOMs approach does not ensure geographical continuity, so any singular grid point is manually added to the final region. The boundaries we identify for the NAM region are similar to those which emerge in the US Southwest from the work of Swenson and Grotjahn (2019) (their Fig. 7), and cover all of Arizona and part of California, Nevada, Utah, Colorado and New Mexico. The differences in the western and northern boundaries (compared to their results) are attributed to sensitivity of the method to the addition of grid points outside of the CONUS.

Although the overall NAM domain emerges naturally from this SOMs analysis, further delineation of precipitation subregions is still necessary given the domain's heterogeneous geographical and topographical characteristics. The same SOMs-based approach is again applied to the identified NAM region, but instead of the all-year long-term daily mean, only the summertime precipitation (June, July, August and September) is used as input. Figure 2 depicts the 7 subregions identified from SOMs, along with their LTDM precipitation signals. Subregions 1 through 7 (Sub1-Sub7), respectively, refer to: (1) the southern half of the Baja California Peninsula; (2) Southeastern California, Northern Sonora and Eastern Arizona; (3) southwestern Utah and most of southern Nevada; (4) the Colorado Plateau and the 'Four Corners' region; (5) most of the Arizona desert, New Mexico and Northern Chihuahua; (6) most of Sonora; and (7) Southern Sonora and Northern Sinaloa. Comparing the LTDM precipitation signal in each region, it is clear that coastal areas such as Sub7, and Sub6 are wetter regions, with higher overall precipitation rates, while the inland deserts are relatively drier (e.g., Sub2 and Sub3). It is also clear that the timing of the shift to the wetter monsoonal precipitation regime varies by subregion. Throughout the literature, the precise definition of monsoon onset date varies: it is derived as the first day after June 1^{st} when precipitation rate exceeds 0.5 mm/day and lasts for 3 days in R. Higgins et al. (1997), while the threshold is 1 mm/day and 5 consecutive days in Turrent and Cavazos (2009). This difference is primarily due to the area of interest: Turrent and Cavazos (2009) examined the whole NAM area, whereas R. Higgins et al. (1997) focused on New Mexico and Arizona, where the climatological precipitation signal is weaker. We adopt 1 mm/day and 5 days here, yielding median monsoon onset dates for Sub1-Sub7 of Aug 30^{th}, July 30^{th}, July 20^{th}, July 19^{th}, July 6^{th}, July 4^{th} and June 30^{th}, respectively. The onset dates are generally earlier for more southern subregions, with Sub1 being a clear exception. The late onset date here is attributed to the impact of tropical cyclones (TCs), as argued in the following sections.

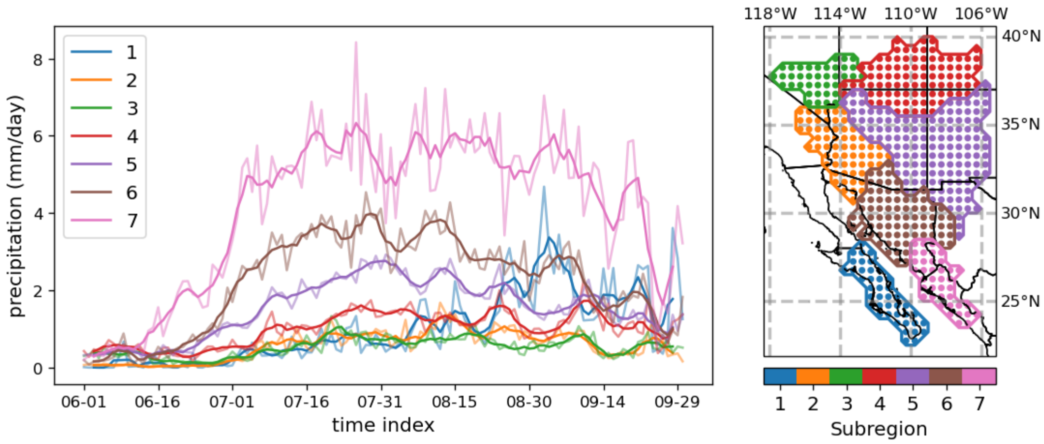

Figure 2. NAM subregions and their long-term daily mean precipitation over summer season. The thin lines represent the long-term daily mean precipitation. For easier visualization, a 5-day mean smoothing is performed to obtain the thick line. The dots denote the grid points from the 0.5° CPC precipitation dataset.

4 Synoptic and Mesoscale Features as Drivers for EPEs

4.1 EPE Definition

Herein, EPEs are defined as days when daily subregion-mean precipitation rate exceeds the 95th percentile of rainy days (i.e., days with precipitation accumulation larger than 1 mm). When consecutive days exceed this threshold, sequential days are consolidated into a single event. As shown in Figure 3, the EPE threshold varies across subregions. What stands out from Figure 3 is the long tail of the distribution. This is especially true for Sub1; its EPE threshold is higher than that of Sub7, while Sub7 is wetter overall, with higher mean precipitation rates during rainy days (6.41 mm/day for Sub7 and 5.99 mm/day for Sub1). Additionally, the long-term daily mean precipitation rate is higher in Sub6 than Sub1, as shown in Figure 2, yet the EPE threshold is much higher in Sub1. These differences highlight the discrepancy between precipitation climatology in the mean and the tail, and supports the need for subregion delineation.

Figure 4 shows the number of EPEs in each subregion from 1979 to 2018. Since the coastal regions have more rainy days, following our criteria, they also tend to have more EPEs. A Mann-Kendall (MK) test is applied to each subregion to see if there is a historical trend in the number of EPE events, EPE precipitation amount, and EPE precipitation rate each year from 1979 to 2018. This test has been shown to be effective in detecting monotonic trends in precipitation analysis (F. Wang et al., 2020). Note that EPE precipitation rate is defined here as the EPE precipitation amount divided by the number of extreme precipitation days, which is not the same as the number of EPE events when there are consecutive extreme precipitation days. In most subregions, there are no significant trends at the 5% confidence level, however, EPE event numbers and precipitation amount do exhibit a significant increase in Sub1 and Sub6. Sub1 also shows a rising trend in EPE precipitation rate, while Sub2 shows a declining trend. These changes are likely influenced by a combination of low-frequency climate variability and climate change.

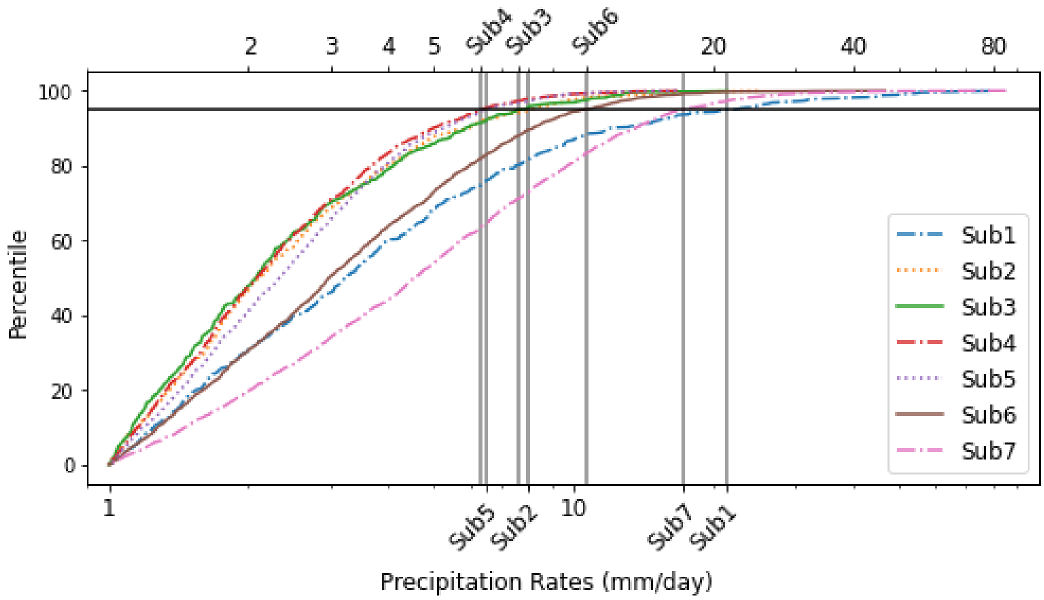

Figure 3. Cumulative subregion precipitation rate distributions. The percentiles are shown on the Y axis. The black horizontal lines represent the EPE threshold (i.e., the 95th percentile of precipitation rate).

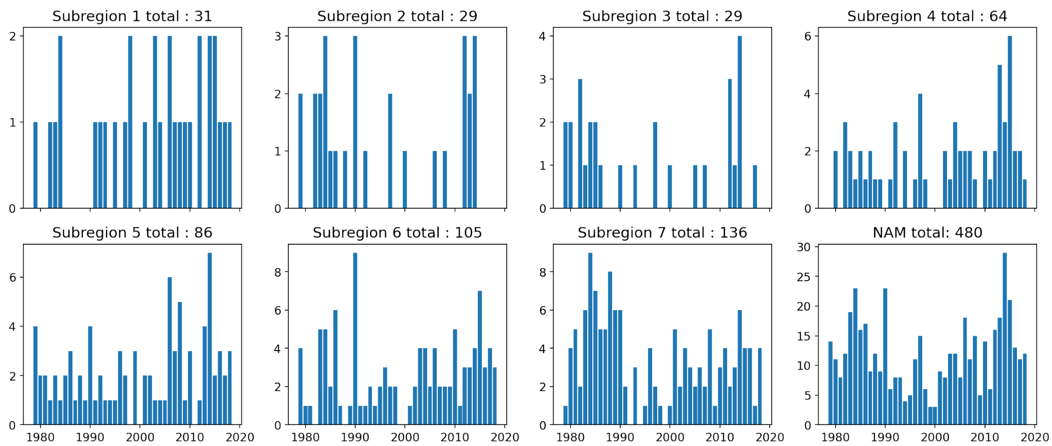

Figure 4. Number of extreme events in each subregion for each year, and total number of extreme events over all subregions.

4.2 Selected Features

For the purposes of identifying the process drivers of EPEs in the NAM region, we select and examine five synoptic features and one mesoscale feature: tropical cyclones (TC), Gulf of California moisture surges, upper troposphere troughs (UTT), frontal systems, mid-tropospheric lows, and mesoscale convective systems (MCS). These features are selected based on previous studies connecting them with EPEs (e.g., Kunkel et al. (2012), Catto et al. (2012), Barlow et al. (2019), and Sierks et al. (2020)). The following subsections introduce each feature and corresponding procedures to link these events with EPEs.

4.2.1 Tropical Cyclones

Tropical cyclones (TCs) are prominent extreme phenomena in the global hydroclimate system. They transport significant water vapor from the tropics and sub-tropics, and account for a large fraction of EPEs around the world (Zhao, 2022). In the NAM region, previous studies have demonstrated that TCs are major contributors to precipitation over Baja California and Northern Mexico (Englehart & Douglas, 2001; Díaz et al., 2008). In this study, TC tracks from the International Best Track Archive for Climate Stewardship (IBTrACS) are used (Knapp et al., 2010, 2018). IBTrACS provides 3-hourly records of TC locations and intensities around the world from 1842 to present (Knapp et al., 2010). We exclude tropical depressions (TDs) from this analysis, selecting only tropical storms (TSs), tropical cyclones (TCs), and hurricanes (HRs). A TC is linked to an EPE if its track is within a 5-degree radius of the given NAM subregion. This distance criterion is based on the general horizontal scale of TCs (Jiang & Zipser, 2010; Kunkel et al., 2012; C. Dominguez & Magaña, 2018).

4.2.2 Gulf of California Moisture Surges

As discussed in Bordoni and Stevens (2006), precipitation variability in the NAM region is strongly connected with northward surges of vapor transport along the Gulf of California (GOC). GOC moisture surges boost continental humidity, provide the necessary water vapor for precipitation, and decrease the moist convective stability of the environment. In F. Dominguez et al. (2016), a simulation using the Weather Research and Forecasting Model with water vapor tracer diagnostics (WRF-WVT) examined the origins of water vapor that contributes to precipitation during the NAM season. The sources were divided into four regions: two marine sources including Gulf of Mexico (GOM) and GOC, and two terrestrial sources including Sierra Madre and the NAM region, defined as regions in the east of Sierra Madre. From their 10-year simulation, they concluded that advected moisture from the GOC was the greatest contributor to non-locally-sourced precipitation in the NAM region.

GOC moisture surges are identified using the vertical integral of northward and eastward vapor flux (denoted as IVT-N and IVT-E) from ERA5 6-hourly reanalysis data. Figure 5 shows the GOC transect with grid points aligned along the gulf in a 25-km spatial resolution. The northward and eastward fluxes are reconstructed as fluxes parallel to (IVT-A) and perpendicular to (IVT-B) the GOC transect, and the grid points along the perpendicular axis are averaged to derive a one-dimensional flux profile along the Gulf. Surge candidates are defined as fluxes that surpass the 95^{th} percentile of vapor flux at each grid point. The spatio-temporally consecutive candidate grid points are then characterized as a surge event, which must last at least 12 hours. The detection method is illustrated in Figure 6 with four surge events shown.

Figure 7 shows the precipitation anomalies with respect to the surge occurrence. The x-axis denotes days after the onset of surges with negative values representing days before the surge and positive for days after the surge. Zero denotes the surge onset date.

Figure 5. The GOC transect grid points.

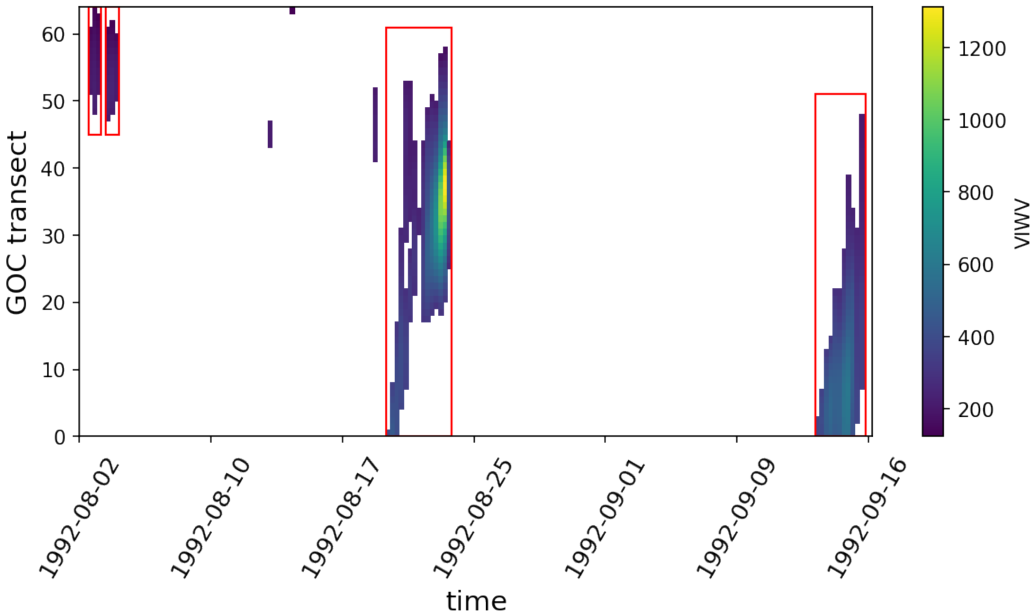

Figure 6. Examples from 1992 GOC surge detection result in Hovmoller diagram. Only the candidate surge grid points are shown. A surge is identified as a continuous band in the figure, and is denoted with a red box. Four surge events are identified in this figure. The specific candidate grid points are not included.

Most subregions show precipitation peaks 2 or 3 days after the onset date while Sub7 shows double peaks, with the first peak on the onset date; this behavior is due to its location at the southern end of the GOC. In addition, the precipitation anomaly is negative on the onset date in Sub3, Sub4 and Sub5, suggesting dry conditions prior to surge arrival. An EPE is deemed to be driven by a GOC surge if the criteria for a surge occurs within a specific time window before the EPE. The window size is set to 0 days for Sub7, 1 day for Sub2, 2 days for Sub1, Sub3, Sub4, and Sub5, and 3 days for Sub6.

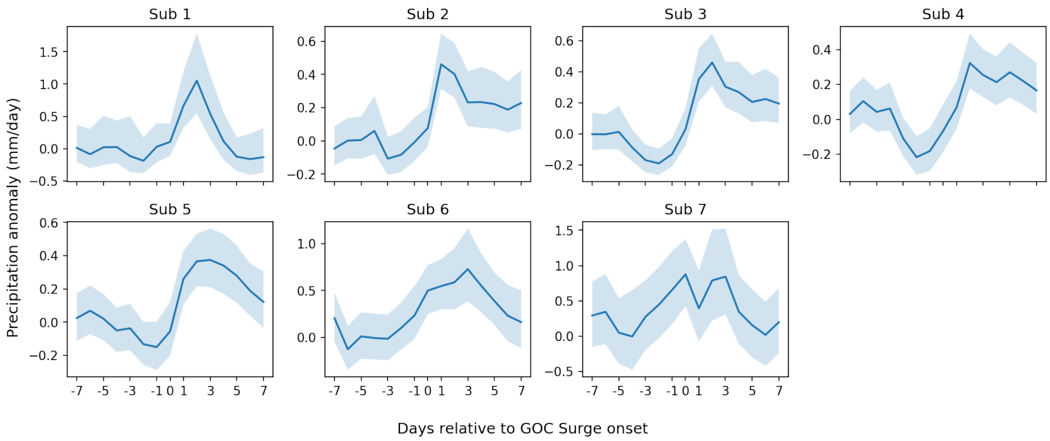

Figure 7. Precipitation anomaly composites of GOC Surges. Shading indicates the 95% confidence intervals, generated by bootstrapping.

4.2.3 Upper Troposphere Troughs

Upper troposphere troughs (UTTs) are upper-level circulation patterns with a local low geopotential height and high potential vorticity around 200 hPa (Kelley & Mock, 1982). Among the subtypes of UTTs, Rossby wave breaking events (RWBs) and inverted troughs (ITs) are perhaps the two features most commonly employed in precipitation analysis. RWBs are often characterized by a reversal in the latitudinal PV gradient near the tropopause (Zavadoff & Kirtman, 2019). When the length-width ratio of PV overturning is large, it is also referred to as a PV streamer (Papin et al., 2020). The effects of RWBs and ITs on precipitation in the Lake Mead Watershed were explored in Sierks et al. (2020). RWBs have also been linked to precipitation in Ryoo et al. (2013), who showed a strong correlation between PV200 and precipitation. Moore et al. (2019) also links EPEs with RWBs, and according to their findings, the majority of EPEs in the central and eastern United States are associated with concurrent PV streamers from RWBs. In contrast to RWBs, an IT is a trough with pressure increasing toward the poles, which is opposite in structure to the most common mid-latitude troughs. For the NAM region, tropical upper-troposphere troughs (TUTTs) are the most common IT type. TUTTs, unlike RWBs, are more common in subtropical easterlies, albeit they are also connected to mid-latitude wave breaking events (Igel et al., 2021). To assess their impact on precipitation, Finch and Johnson (2010b) utilized quasigeostrophic (QG) theory to study a TUTT event over the NAM region in July 2004. Newman and Johnson (2012) used WRF to simulate the same event. Their results showed wind shear and convective available potential energy (CAPE) both increased during the TUTT event, particularly to the west of the TUTT. TUTT-induced convective enhancement was also identified in Bieda III et al. (2009), where it was shown that lightning event density increases when a TUTT is present. Interactions between TUTTs, RWBs and TCs were also investigated in Z. Wang et al. (2020). A comprehensive TUTT dataset was built based on the 200 hPa stream

Table 1. Number of UTT-EPE events by propagation direction in each subregion.

	Sub1	Sub2	Sub3	Sub4	Sub5	Sub6	Sub7
UTT events	10	15	12	33	51	46	53
Westward	6	9	2	8	21	36	35
Eastward	4	6	10	25	30	10	18

function in Igel et al. (2021), and their composite analysis showed an enhancement in precipitation to the southeast of the TUTT core.

The wide variety of upper level disturbances (RWBs, PV streamers, TUTTs, ITs) all exhibit a local high in potential vorticity at the tropopause, commonly approximated by the 200 hPa level. In this study, UTT candidates are first identified as closed contours of $2{\times}10^{-6}\ m^2s^{-1}Kkg^{-1}$, or 2 PVU from the ERA5 6-hourly 200 hPa potential vorticity by TempestExtremes (Ullrich et al., 2021). A filter is applied on prospective UTT candidates to remove coincident TCs, to ensure that we only extract upper-level disturbances.

To better examine the effect of UTTs on regional precipitation, we composite precipitation anomalies (i.e., precipitation minus its long-term daily mean) within a 20-degree radius of each tracked UTT in Figure 8. The radius of 20 degrees is large enough to capture possible longer-range UTT impacts on precipitation. Only anomalies that satisfy a 95% confidence interval derived with a two-sided Student's t test are plotted. Precipitation is consistently depressed to the north and northeast of the UTT center, and enhanced to the south and southeast. Within 10 degrees, the enhancement reaches its peak and diminishes with distance. As we previously noted, UTTs include both mid-latitude disturbances (RWBs) and tropical features (i.e., tropical UTTs or TUTTs). To examine these two types of UTTs, we separate the UTTs by their direction of propagation, and compose feature-centered precipitation in Figure 8, along with geographically-fixed PV200 and U200 for eastward and westward propagating UTTs. Figure 9 shows these composites in Sub6, as an example. Unsurprisingly, the propagation direction of the upper-level disturbances is generally determined by the large-scale background flow. PV200 shows positive anomalies in extratropical regions for eastward-moving UTTs, and the high PV200 disturbances are located in the extratropical westerlies. This behavior aligns with the RWB features in Zavadoff and Kirtman (2019). In contrast, the positive PV200 anomalies are relatively smaller for westward-moving UTTs, and they are located in the tropical easterlies. This follows Igel et al. (2021), where it is argued that TUTTs are advected by the background easterlies. Moreover, the boundary of westerly and easterly flow moves further north during westward-UTT events. This transition favors TUTT advection from the tropics to the NAM region, and indicates that eastward-UTT related EPEs are more frequent for northern NAM subregions, as shown in Table 1. Thus, although we use UTT as a category for all upper-level disturbances, they can be classified into tropical and subtropical features based on their location and direction of propagation.

Westward- and eastward-moving UTTs lead to very different precipitation anomalies, as shown in the precipitation anomaly composites (as in Figure 8). Eastward UTTs exhibit enhanced precipitation to the southeast of the feature and suppressed precipitation in all other quadrants. On the other hand, the westward UTTs exhibit scattered and weak enhancement of precipitation to the south and stronger suppression of precipitation to the northeast. Despite these differences in behavior, the precipitation enhancement is still within 10 degrees of the UTT center for westward UTTs and so 10 degrees is set as the criterion for UTTs. That is, if there is a concurrent UTT in the 10-degree radius from the subregion, the EPE will be assigned to this UTT. This disparity in precipitation composites as shown in Figure 8 is further discussed in the following sections.

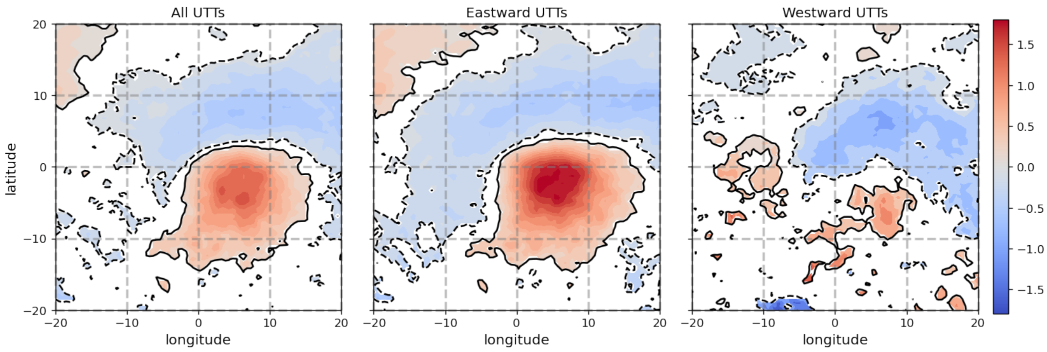

Figure 8. UTT-centered composites of precipitation anomalies with confidence level at 95%. Colors show the precipitation anomaly in mm/day. Solid and dash lines are for confidence interval contours.

4.2.4 Frontal Systems

Frontal systems, especially in the mid-latitudes, promote precipitation by inducing uplift. Catto et al. (2012) describes the importance of frontal systems for precipitation around the world, arguing that they are responsible for 46 percent of overland precipitation in the Northern Hemisphere. According to Kunkel et al. (2012), 44 percent of EPEs in the southwestern US summertime are attributable to frontal activities.

Despite the existence of automated identification methods for frontal systems, available schemes either require substantial computational power (Hewson, 1998), or are insufficiently validated over the NAM region (Parfitt et al., 2017; Biard & Kunkel, 2019). Instead of identifying fronts from reanalysis data, we use a manually labeled dataset from National Weather Service (NWS) coded surface bulletins. From 2003, this NWS dataset provides the locations and types of frontal systems at 3-hour intervals, which are determined by a National Weather Service meteorologist (Biard, 2019). To link EPEs with frontal systems, we use the method from Catto et al. (2012): If a concurrent front is 5 degrees or less away from the EPE area, the EPE is associated with that front.

4.2.5 Mid-tropospheric Lows

Often, moisture transport is driven by mid-tropospheric (i.e., 500 hPa) disturbances that do not strongly manifest at the surface level or in the upper atmosphere. Wibig (1999) used 500 hPa geopotential height to identify circulation patterns related to winter precipitation over the Euro-Atlantic sector. The atmospheric circulation patterns related to EPEs over Greece emerged by analyzing the clustering results of 500 hPa geopotential height fields in Houssos et al. (2008). In this study, we detect anomalous lows at the 500 hPa level and assess their importance as a driver of EPEs. The composite mean of 500 hPa geopotential anomaly during EPEs is shown in Figure 10. The low centers are generally located to the west of the inland subregions, and the anomalies are weaker for coastal subregions, though all features are significant at the 95% confidence level. Based on this analysis, where a concurrent $\Phi 500$ anomaly low stronger than -1000 m^2/s^2 is less than 5 degrees away from the subregion, the EPE is associated with a mid-tropospheric low.

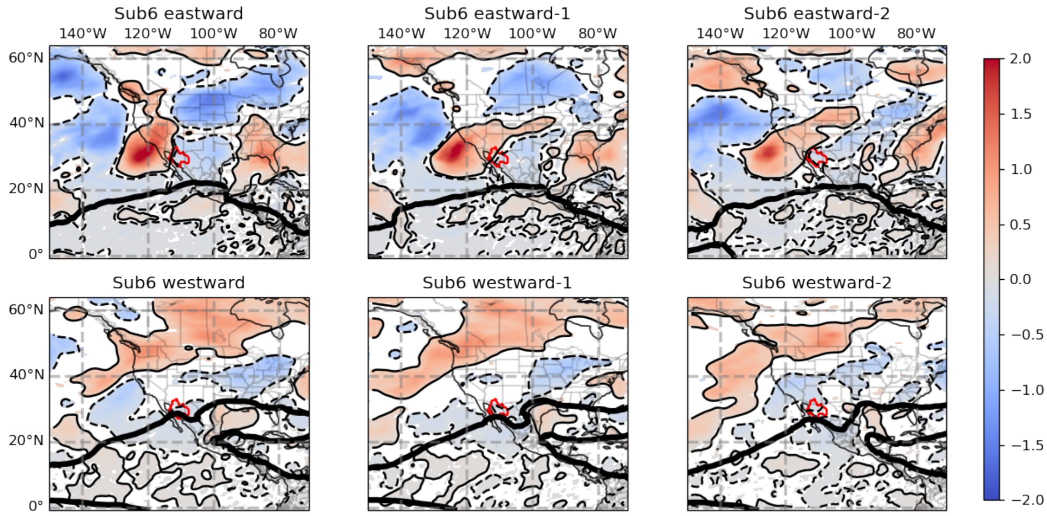

Figure 9. PV200 standardized anomalies and zero U200 contour for eastward and westward UTTs in Sub6. The red polygon denotes the location of Sub6. The solid black contour represents the line of zero 200 hPa zonal wind, separating easterly and westerly winds. Shading depicts PV200 standardized anomalies within a 95% confidence interval. The left column is the composite of all days concurrent with the UTT event. The middle and right columns are for one day prior and two days prior to the onset date, respectively.

4.2.6 Mesoscale Convective Systems

Mesoscale convective systems (MCS) are significant drivers of global precipitation (Zhao, 2022). Specific to the NAM region, Finch and Johnson (2010a) and Mejia et al. (2016) used observational records to show that MCS activity increases over the summer in the NAM region. While MCSs are difficult to resolve in modern reanalysis data, a variety of observational products possess sufficiently high resolution to enable MCS detection. Feng et al. (2021) tracked MCSs globally based on infrared brightness temperature and precipitation from satellite datasets from 2001 onward. In this study we analyzed a subset of this tracking data covering the NAM region. A MCS event is deemed to be associated with an EPE only if there are labeled MCS grid points inside the precipitating area.

4.3 EPE Feature Drivers and Trends

Since the frontal system record starts from 2003 and the MCS dataset is available from 2001, only TCs, UTTs, GOC surges and mid-tropospheric lows are considered for EPEs before 2003. Fronts and MCS are included for events from 2003 onward. Figure 11 shows the precipitation amount fraction with different drivers for EPEs before and after 2003. The fraction of EPE numbers associated with the candidate drivers are depicted in Figure 12. The events that are not linked with any candidate drivers are denoted as ‘unclassified’ (abbreviated as ‘Unclass’). Although there are several unclassified events before 2003, the inclusion of frontal systems and MCSs leads to only one unclassified event since 2003. This suggests that the features identified in this study are fairly comprehensive as EPE drivers.

For most subregions, GOC surges and fronts are the two leading drivers, and account for both more relevant events and larger precipitation amounts. TCs have a greater

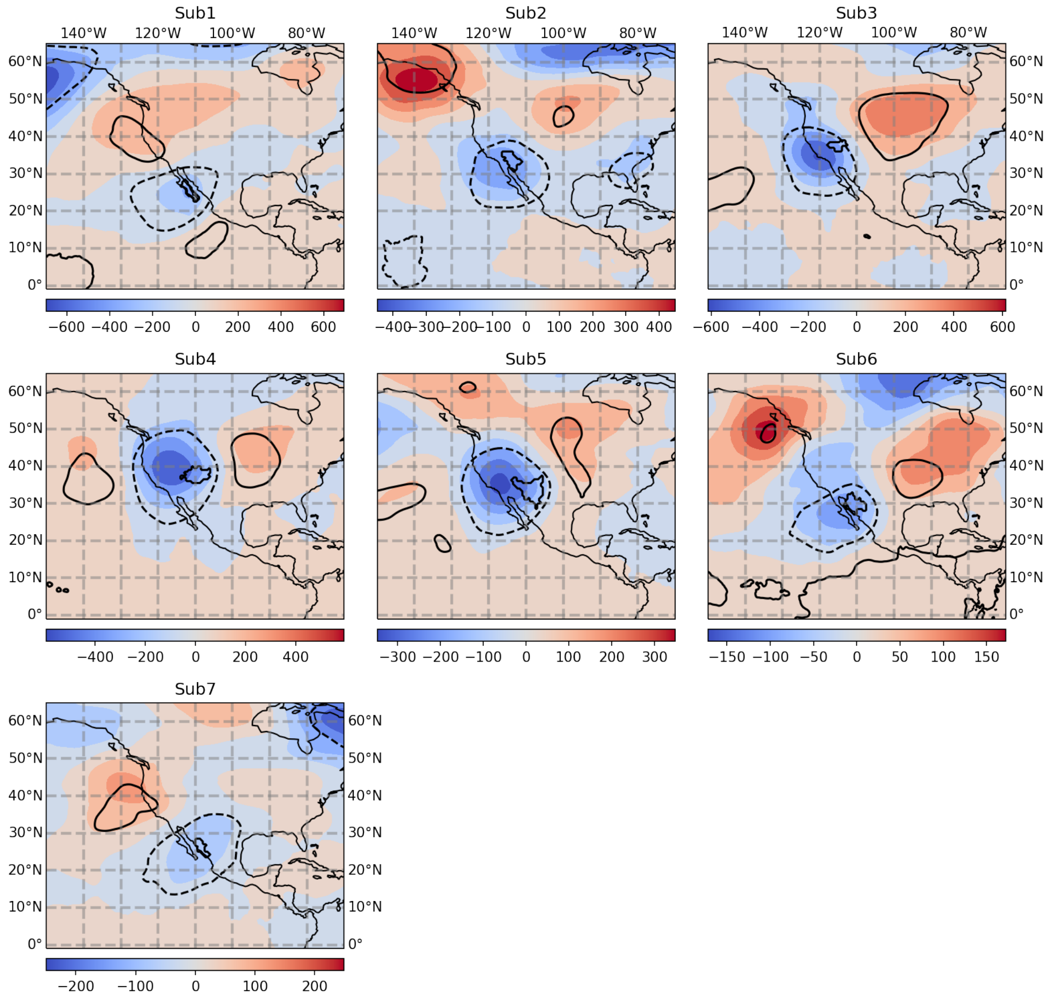

Figure 10. EPE 500 hPa geopotential anomaly composites. Black contours denote the 95% confidence interval (the solid line denotes positive anomalies and the dashed line denotes negative anomalies).

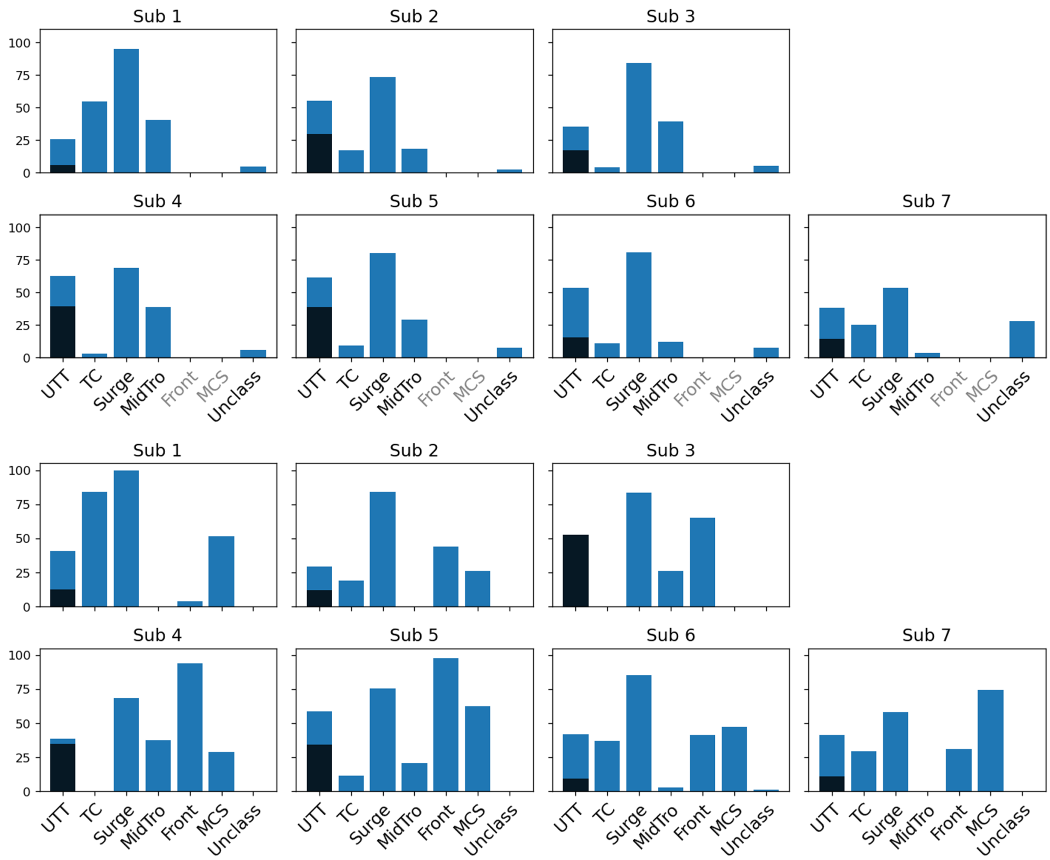

Figure 11. EPE precipitation amount (%) associated with different feature drivers before (top) and after (bottom) 2003. The black color denotes eastward-UTTs. Since a given EPE could be associated with more than one feature, the percentages do not add up to 100%. Fronts and MCSs are not associated with EPEs prior to 2003.

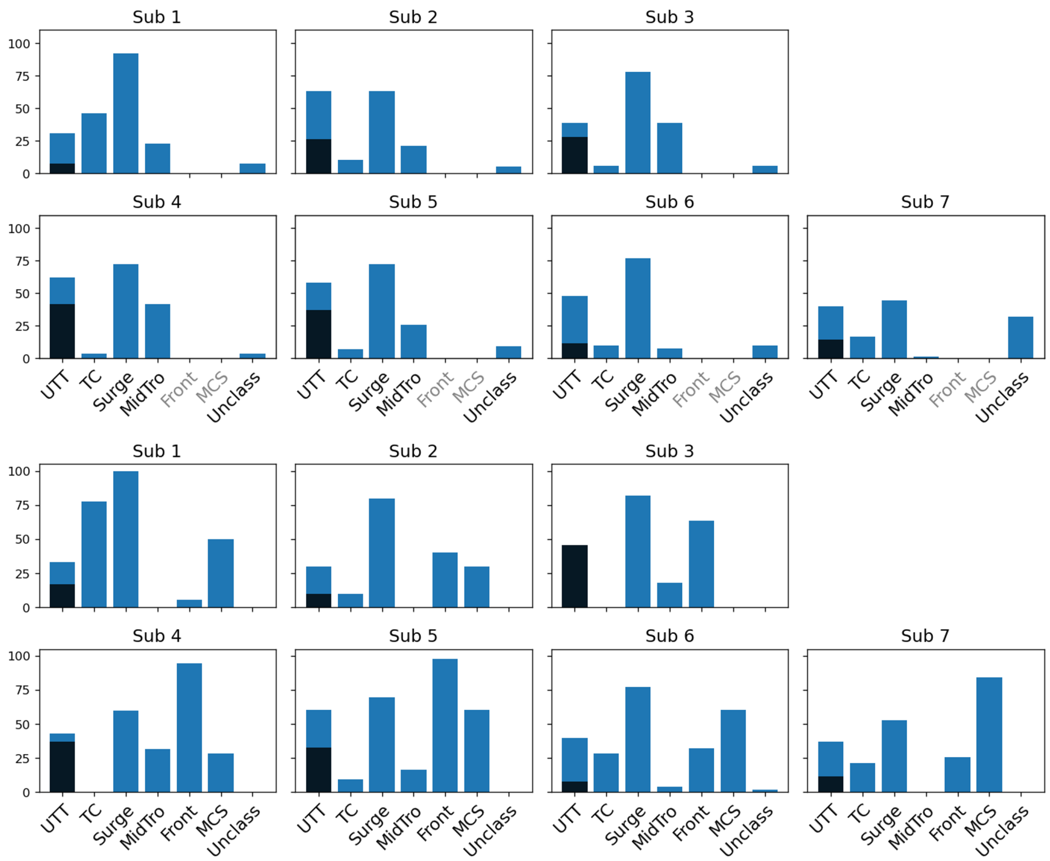

Figure 12. Similar with Figure 11, but for EPE occurrence percentage (%).

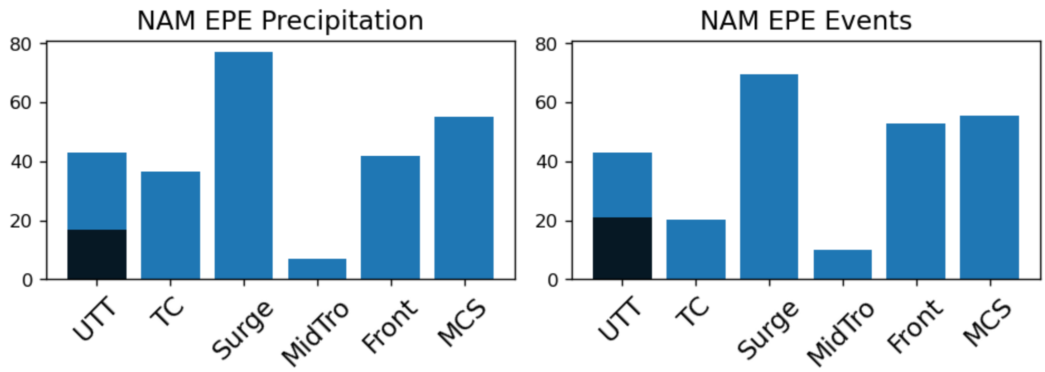

Figure 13. EPE precipitation and event fraction associated with different drivers for the whole NAM region after 2003. The black color denotes the eastward-UTTs.

impact on Sub1 and Sub6, and MCSs dominate Sub7. Mid-tropospheric lows are more frequent drivers of EPEs over inland subregions (Sub3, Sub4 and Sub5) than coastal areas, which is consistent with Figure 10 where the geopotential low is more pronounced in these subregions. In addition to Figure 11 and 12 showing EPE attribution for each subregion, Figure 13 aggregates the driver attribution over the whole NAM region. Over the whole domain, the precipitation amount and EPE fraction are similarly ranked, with surges being the most dominant driver and MCSs coming in second. Despite the fact that only about 20% EPE events are linked to TCs, TCs are associated with almost 40% of EPE precipitation, which highlights the substantial precipitation amount that each TC-EPE produces.

It should be noted that the feature classification in Figures 11, 12 and 13 is not exclusive (i.e., a UTT event can also be linked with other drivers like GOC surges or MCS). Combined events (i.e., two features simultaneously) are further investigated with EPEs after 2003, since all but one of the EPEs can be assigned to at least one candidate driver. The results are illustrated in Figure 14. In general, most of the EPEs are caused by two to three drivers. However, there are fewer categories in Sub1, Sub2 and Sub3, while the interactions are more complex in Sub6 and Sub7.

Perhaps what stands out the most are those events induced solely by a single driver. Particularly for Sub7, MCSs are the dominant driver of EPEs, with the EPE precipitation solely driven by MCSs exceeding 10% (Figure 14), and about 65% coming from MCSs combined with another feature (Figure 11). This result indicates the importance of MCSs in this area as a driver for EPEs, and explains why this region suffers from a large percentage of 'Unclassified' events before 2003. Fronts are another feature unavailable in our analysis before 2003, and one that is particularly important over inland subregions (Sub2, Sub3 and Sub4), where the front-only EPE precipitation exceeds 5%. In contrast with MCSs and fronts, TCs are an important feature for EPEs yet never occur by themselves; almost all TC-related EPEs occur in conjunction with GOC surges. Mid-tropospheric lows are also closely associated with frontal activity – in fact, all EPEs associated with mid-tropospheric lows after 2003 are also associated with fronts, suggesting some redundancy in tracking these features. For Sub3 to Sub6, where fronts and mid-tropospheric lows are frequent, the frontal system types are examined against the existence of mid-tropospheric lows. As listed in Table 2, although not all fronts with mid-tropospheric lows are cold fronts, the proportion of cold fronts increases when mid-tropospheric lows are present.

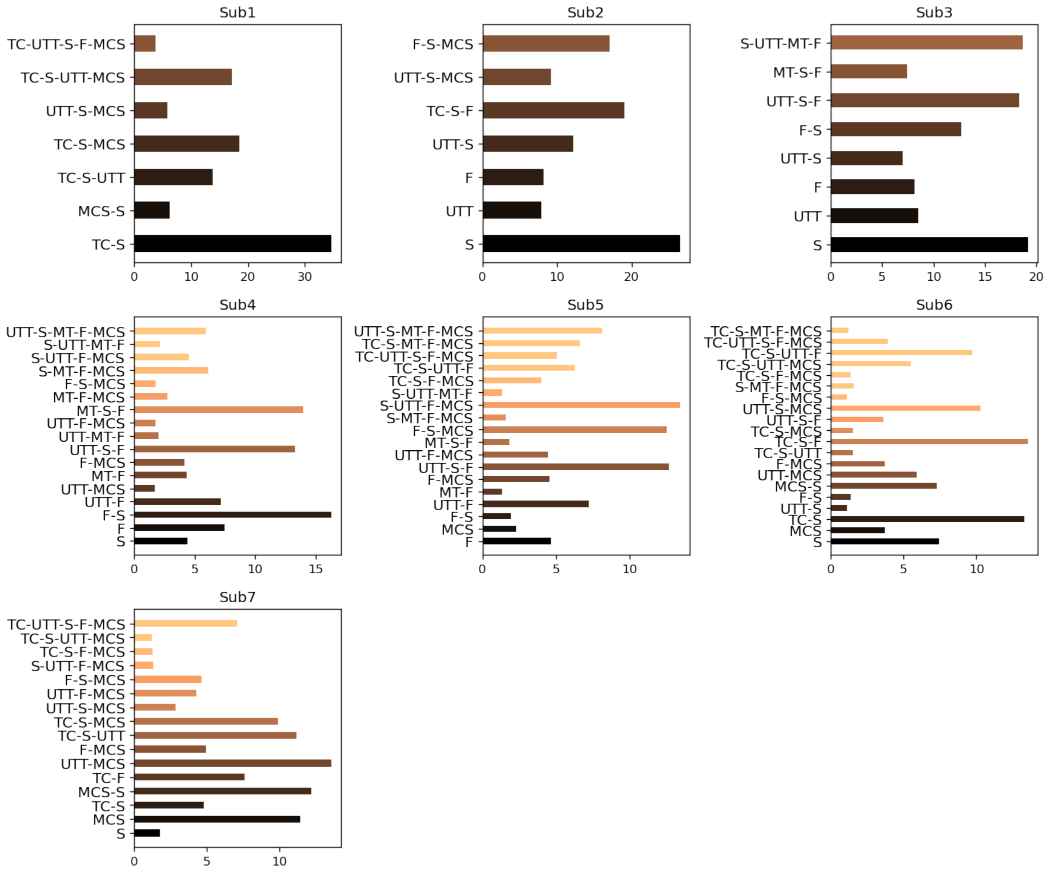

Figure 14. Combinations of different drivers for EPE precipitation after 2003. The bar length represents the fraction of EPE precipitation amount. The abbreviation 'UTT' refers to upper-troposphere troughs, 'F' to fronts and 'S' to GOC surges.

Table 2. Type of frontal system present with and without an associated mid-troposphere low.

	Sub3	Sub4	Sub5	Sub6
Without Mid-tropospheric Lows				
Cold Fronts	3	6	10	4
Stationary Fronts	2	20	35	15
With Mid-tropospheric Lows				
Cold Fronts	3	8	5	1
Stationary Fronts	0	5	7	1

As shown previously, key EPE metrics (both number of EPEs and EPE precipitation amount) have increased in Sub1 and Sub6, while EPE precipitation rate has trended down in Sub2. Since we have now classified EPEs by feature type, the trends for each EPE category in these three subregions are further examined with the same MK test. Since 6 categories are being tested at the same time, a Bonferroni correction is applied to adjust the confidence level from 0.05 to $0.05/6 \approx 0.008$.

For the number of EPEs in each year, only the trend in TC-related EPEs is significant in Sub6 – there are no significant trends for other categories or regions. Although an upward trend in the number of EPEs is found in Sub1, none of the EPE categories have increased significantly, likely due to the strict p-value from Bonferroni adjustment (Perneger, 1998). The likely culprit is thus the number of TC-EPEs in Sub1, which has an increasing trend with a p-value of 0.010, much lower than other categories. The trend in precipitation amount is only significant for TC-EPEs in Sub1 and Sub6, and there are no significant trends for the remaining categories. Only Sub6 exhibits an increasing trend for TC-EPE precipitation rate, and again the p-value (0.012) for TC-EPE precipitation rate in Sub1 is the lowest among all the categories, but not significant with the Bonferroni adjustment. This result suggests that the significant trends of EPE numbers and total precipitation in Sub1 and Sub6 are explained by an increase in TC-related EPEs and their associated precipitation rates. The increasing trend in TC-EPE precipitation rates is indicative of more intense TC rainfall. The upward trend in TC-EPE numbers may be affected by low-frequency variability (Pazos & Mendoza, 2013), or global warming, (i.e., the observed increase in TC frequency over Baja California (Murakami et al., 2020) and in the eastern North Pacific (Klotzbach et al., 2022)). But it is worth noting that although the increasing trend is significant in Sub6, the rate of change is small with the Theil-Sen slopes being 0 and OLS slopes less than 0.01. A further careful analysis is necessary to better relate these TC trends with potential upstream drivers.

4.4 Meteorological Conditions Driving EPEs

The meteorological field composites for EPEs in each subregion are constructed to reveal the conditions generally present during EPEs. Figure 15 shows the composite for Sub4 as an example. It is unsurprising that EPEs are coincident with moist conditions: all subregions show local high water content in total column water vapor (TCWV) and 850hPa specific humidity (Q850) fields, mostly associated with strong moisture transport over the GOC channel (IVT-A and IVT-B). Similarly, EPEs occur alongside enhanced vertical uplift. Figures for other subregions are available in supplements (Figure S2 to S7). As we discussed in section 4.2.2, when GOC surge onset occurs, Sub4 shows a negative precipitation anomaly, suggestive of a tendency for dry conditions to occur prior to surges reaching Sub4. This is also observed in the concurrent composites, where IVT-A shows negative anomalies for Sub4. The 500hPa geopotential ($\Phi 500$) low center is always present and all the subregions show upward lifting with negative 500 hPa vertical velocity ($\Omega 500$) anomalies. Besides synoptic-scale uplifting, the positive convective available potential energy (CAPE) anomalies indicate a convectively active environment. Both the moisture and vertical ascent create a favorable environment for extreme precipitation. In spite of the common patterns of moisture and uplift, the upper-level disturbance exhibits different behaviors across subregions: Sub1, Sub6 and Sub7 (coastal areas) show local anomalous low in PV200, while the strong gradient of PV200 with positive values to the west and negative values to the east is significant in Sub2, Sub3, Sub4 and Sub5 (inland areas). This difference indicates that UTTs (high PV200 contours) are more influential over Sub3, Sub4 and Sub5, which is consistent with the higher UTT-EPE precipitation fraction over inland areas in Figure 11. There are also magnitude differences across the subregions. Taking TCWV and Z500 as examples, composite magnitudes are relatively larger for inland areas like Sub3 and Sub4 compared with Sub6 and Sub7 (Figure S8 and Figure S9). This is probably due to the fact that MCSs are more

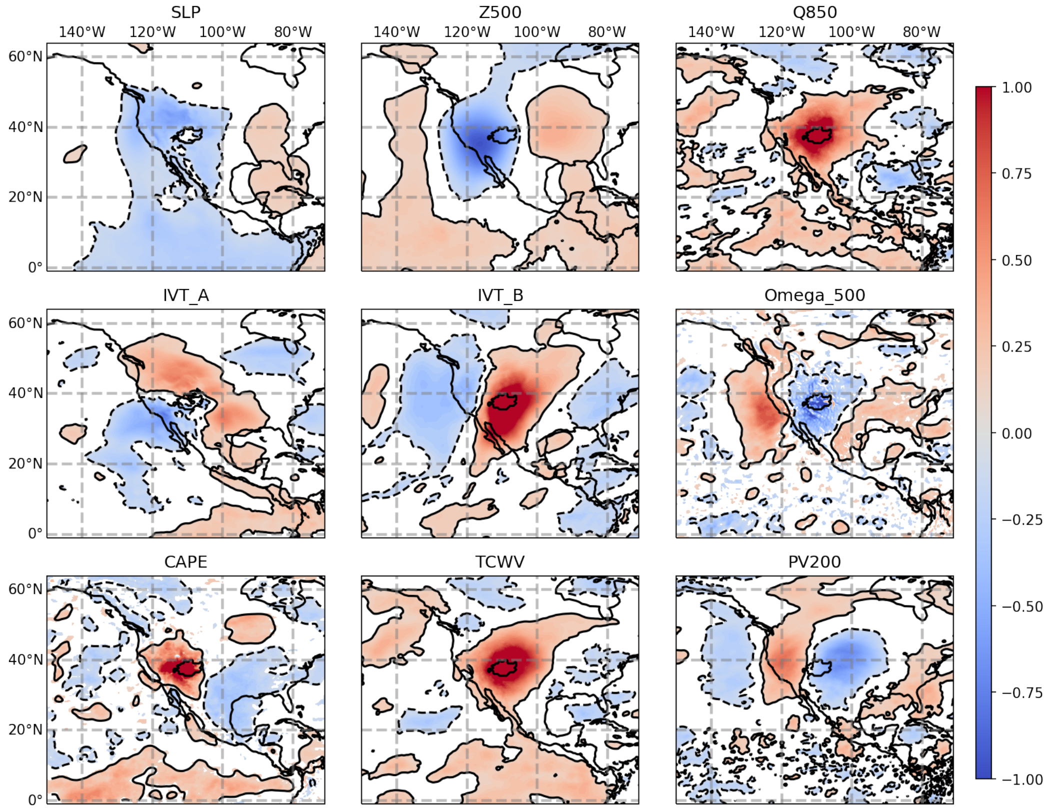

Figure 15. Standardized anomaly composites of EPE events in Sub4. Composites are shown at 95% confidence intervals derived from a two-sided t-test.

important in Sub6 and Sub7, as shown in Figure 11, and occur on scales that are too small to be resolved in these composites.

If we composited all EPEs, the signals from individual EPE drivers would not be apparent and fields would be averaged in each region. Thus, the composites of different EPE categories are further examined and compared. In general, all the drivers exhibit the expected meteorological features that follow from their detection criteria (i.e., the local low SLP and Φ500 for TCs and anomalous positive PV200 for UTTs). Although we have constructed composites for every individual EPE drivers across subregions (Figures S10 to S47), instead of focusing on the meteorology of every singular features, here we examine and contrast several important and similar features.

4.4.1 UTTs and mid-tropospheric lows

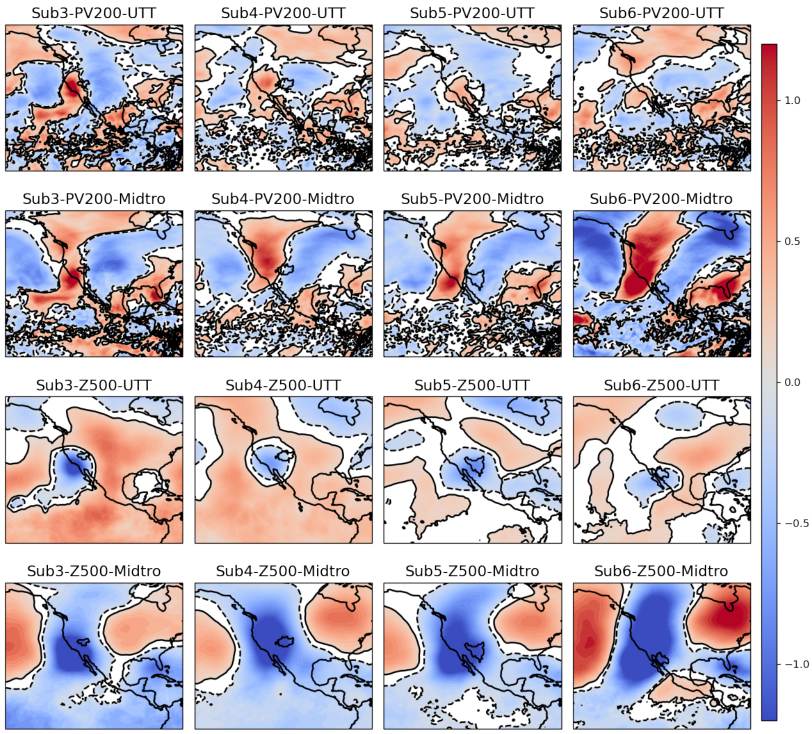

Figure 16. Standardized anomaly composites of UTT and mid-tropospheric lows for Sub3, Sub4, Sub5 and Sub6.

UTTs and mid-tropospheric lows share some common features in PV200 and Φ500, as seen in figure 16, including anomalously high PV200 and low Φ500. Despite these similarities, the anomalies in Z500 and PV200 have a larger horizontal scale for mid-troospheric lows than for UTTs. This is likely related to their horizontal scales: it is suggested that mid-tropospheric lows could be related to planetary Rossby waves and so possess longer wavelengths (Fuentes-Franco et al., 2022), while UTT features are shorter waves that break from the long waves (RWBs), or tropical disturbances, with an average wavelength around 3000km (TUTTs Kelley & Mock, 1982; Chen & Chou, 1994).

4.4.2 Fronts and mid-tropospheric lows

Fronts and mid-tropospheric lows are more frequent in inland subregions (Sub4 and Sub5). As we discussed in section 4.3 and Table 2, mid-tropospheric lows generally have lower surface temperatures as a consequence of the hypsometric equation, which in turn produces a stronger temperature gradient along the periphery of the low; so it is unsurprising that mid-tropospheric lows and fronts are largely co-occurring and should not be considered entirely independent features. As mentioned earlier in our discussion, mid-tropospheric lows are always associated with fronts for EPEs after 2003, as shown in Figure 14. This suggests that features identified as mid-tropospheric lows in our analysis give rise to more intense frontal features. Although both fronts and mid-tropospheric lows can drive uplift, their composites show differences in magnitude and spatial extent. Figure 17 depicts the composites of frontal EPEs with and without mid-tropospheric lows in Sub4. The magnitudes of the anomalies are observed to be larger for fronts with mid-tropospheric lows. In addition, the spatial extent of moisture and upward motion disturbances are greater when mid-tropospheric lows are co-occurring with fronts. This is certainly related to our geopotential magnitude criterion for mid-tropospheric lows; with -1000 m^2/s^2 as the threshold, the trough is deep enough to be generally associated with anomalously low near-surface temperatures. This cold air enhances the temperature gradient and intensifies frontal systems. In addition, as we discussed in section 4.4.1, mid-tropospheric lows are also related to planetary waves, which often have longer wavelength, whereas fronts are more localized. Therefore, larger spatial anomalies are expected associated with mid-tropospheric lows.

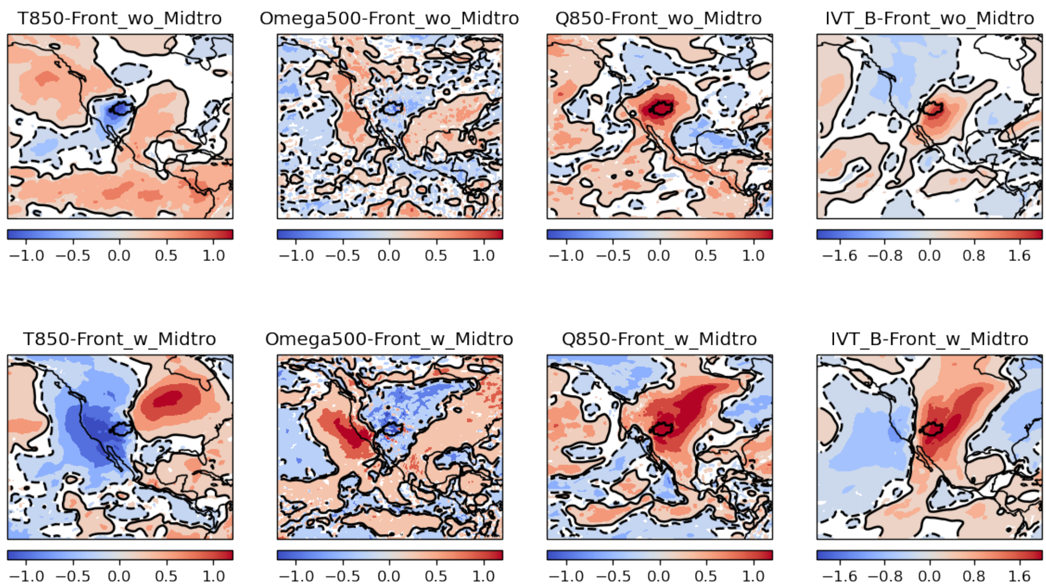

Figure 17. Frontal EPE composites in Sub4. The upper row shows fronts without mid-tropospheric lows and the bottow row fronts with mid-tropospheric lows. The black contours demarcate the 95% confidence interval.

4.4.3 GOC moisture surges

Although winds are largely directed along the GOC in the summertime (Bordoni & Stevens, 2006) and IVT-A is used to derive GOC surges, an enhancement in IVT-B is also observed during GOC surge EPEs as shown in Figure 18, with Sub4 as an example. On the EPE onset dates, the IVT-B anomaly is significant throughout the GOC and

Sub4, while the IVT-A is depressed over GOC and part of Sub4. When examining days prior to EPEs, the positive IVT-A anomalies are observed over GOC 1 day prior and extend larger in space 2 days prior, which follows our window size for Sub4 in Figure 7. In contrast to IVT-A, IVT-B anomalies are consistent in the 3-day window and cover a wider range of spatial locations, including both GOC and Sub4. These results suggest the important role of onshore moisture transport for EPEs, especially over inland areas (e.g., similar composite patterns are observed in Figure S33 for Sub5). Additionally, onshore moisture transport is generally associated with IVT-A, given the location and orientation of the GOC channel, making IVT-A sufficient to represent moisture transport even though it is orthogonal to IVT-B. A further examination shows the correlations between IVT-A and IVT-B are significant, although the coefficients are small. Thus, GOC surges identified solely with IVT-A also suggest an enhancement in IVT-B.

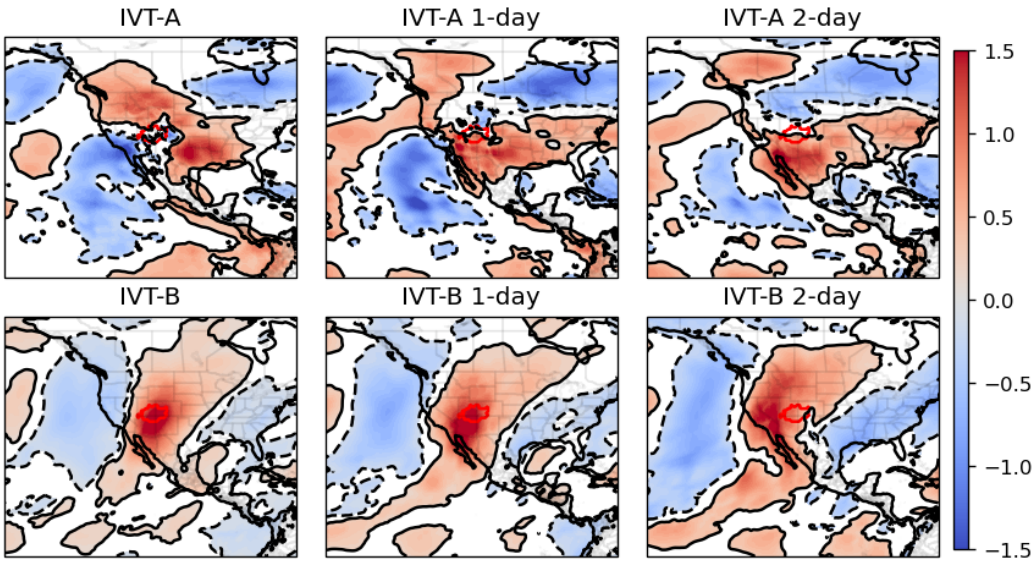

Figure 18. GOC moisture surge EPE composites of standardized anomalies in Sub4. The left column depicts concurrent composites, middle for one day prior and right for two days prior, which is also the GOC surge onset date. Black contours show the 95% confidence interval.

4.4.4 The unclassified EPE of 2003

In addition to the composites for each EPE category, meteorological conditions for the single unclassified event in Sub6 after 2003 are examined and depicted in Figure S48. Local high water content is shown in Q850 fields. PV200 and CAPE indeed show positive anomalies near the precipitation area, and the EPEs are likely related to these disturbances given that there are no clear disturbances found in IVT, SLP and Z500 fields. However, the upper-level disturbance is below 2PVU, which leads to a missed UTT association based on our tracking criteria. As it is associated with a relatively weak upper-level anomaly, it is unsurprising that the precipitation rate of this unclassified event (10.87mm/day) is close to the 95th percentile thresholds (10.65 mm/day).

4.5 Precipitation Rate Distributions Associated with Atmospheric Features

Although we have shown that essentially all NAM EPEs can be associated with a feature driver, the presence of a particular atmospheric driver is, in general, not sufficient to guarantee occurrence of an EPE. To examine precipitation response in the presence of a particular atmospheric feature, we composite the precipitation rate with respect to different drivers and compare the probability of EPEs. Following the definition of rainy days, only those precipitation rates larger than 1 mm/day are analyzed. Although the precipitation rate generally follows a gamma distribution (Watterson & Dix, 2003; Martinez-Villalobos & Neelin, 2019), for precipitation rates larger than 1 mm/day, a generalized Pareto distribution (GPD) is employed since it is widely used for assessing the tail of various distributions (Dargahi-Noubary, 1989). The GPD has three parameters: shape, location, and scale. However, when fitting the data, the location parameter is fixed to 1 mm/day, while shape and scale are optimized using their maximum likelihood estimate.

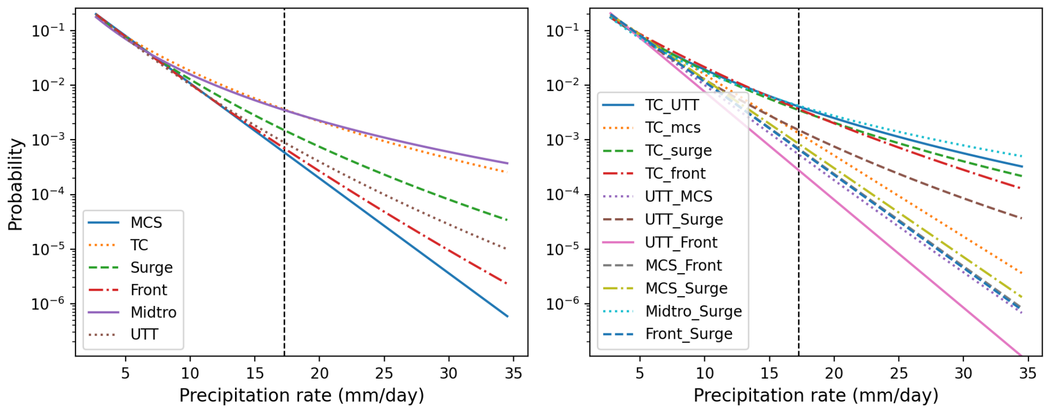

Figure 19. Subdomain-averaged precipitation rate distribution with respect to atmospheric drivers for Sub7. The dashed vertical line denotes the 95$^{\text{th}}$ percentile of precipitation rate. The left panel represents single drivers and the right shows double drivers.

Figure 19 shows the fitted precipitation rate PDF function with single and double atmospheric drivers in Sub7, as an example. Figures for other subregions are available in the supplements (Figure S49 to S54). Overall, a spread emerges in the tail that is strongly dependent on the subregion being examined (i.e., MCSs are more likely to bring heavy precipitation in Sub1 while their precipitation probability is relatively lower in Sub2). While this figure is effective at illustrating this spread, the fits themselves tend to underestimate the probability of extreme precipitation when comparing the CDFs to the observed frequency of EPEs under each feature. Consequently, the area under each PDF above the EPE threshold should not be used to assess EPE probability under each extreme. Thus, we use frequency instead of CDF and utilize bootstrap to derive confidence intervals.

The results of this procedure are shown in Figure 20 for single drivers and the figure for double drivers is available in the supplement (Figure S55). The single driver with the highest extreme precipitation probability is TCs for Sub2, Sub5, Sub6 and Sub7, midtropospheric lows for Sub1 and Sub3, and MCSs for Sub4. Because the probability of EPE occurrence does not incorporate the frequency of each driver, the single driver with the highest extreme precipitation probability is not the greatest contributor to extreme precipitation shown in Figure 11. For example, in Sub5, TCs are the driver with the highest probability of extreme precipitation rates, whereas both the number and precipitation amount of TC-related EPEs are the lowest in Figure 11. This result actually reflects Sub5 being far from the coast and consequently subject to only the most extreme TCs.

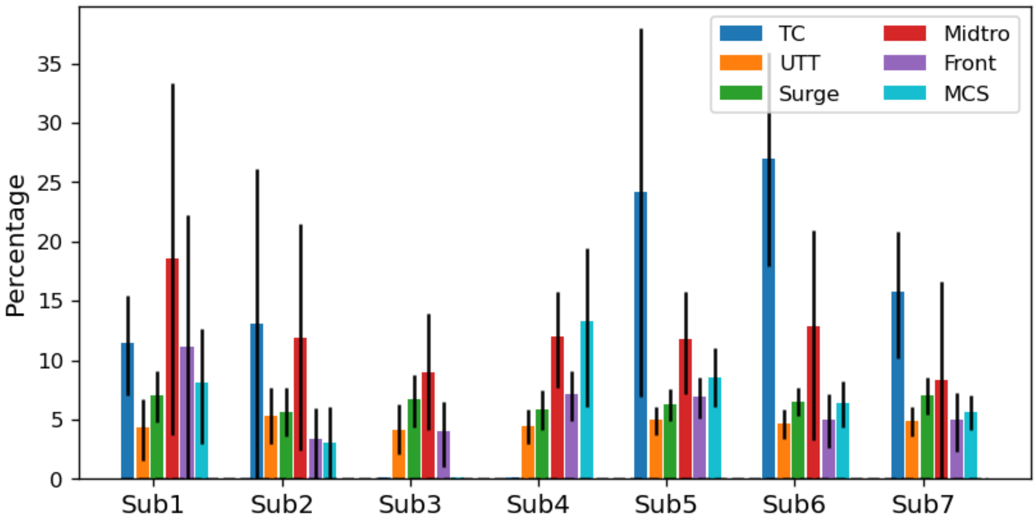

Figure 20. Frequencies of precipitation rates exceeding the extreme threshold associated with the occurrence of single candidate drivers. The error bar shows the 95% confidence interval derived from bootstrap sampling. Probabilities are shown as percentages.

Sub5 is also a desert region with a lower threshold for extreme precipitation compared to coastal areas like Sub1, Sub2, Sub6 and Sub7 (Figure 3).

Compared with the single drivers, the probability for an EPE to occur when two drivers are present is not necessarily higher with the addition of another driver (e.g., the probability of TC-Midtro in Sub6 (0.20) is less than TC (0.27)), implying that the multi-driver interactions are not always additive. When the second driver is included, the extreme precipitation probability may increase, decrease or remain unchanged, depending on the subregion and associated drivers. In the remainder of this section, we investigate some more interesting combinations of features. Since the sample size is limited, the confidence intervals for the EPE probabilities are wide, indicating a large uncertainty associated with the frequency. Thus, instead of frequencies as single scalars, we instead perform a qualitative assessment using the GPD PDF functions, especially for the high precipitation rate regime.

4.5.1 TC-Surge interactions

Given their close association, it is perhaps unsurprising that TC and TC-Surge PDF curves are similar in Sub1 and Sub7 as shown in Figure 21. In addition, the number of TC-Surge-related precipitation days is about equal to the number of TC-related days, indicative of TCs being closely associated with GOC surges. As Sub1 and Sub7 are towards the south end of GOC, the precipitation response to TCs and TC-Surges are nearly identical in these regions.

4.5.2 TC-UTT interactions

The PDF curves for TC, UTT and TC-UTT precipitation are further compared in Sub7 since TC and UTTs are both frequent here. In Figure 21, the TC-UTT-10° (i.e., TC-UTT double driver using the default 10 degree UTT search radius) precipitation curve is close to the TC curve, while the UTT-10° curve is far below these two curves, indicating much lower probability of high precipitation intensity. The insignificant impact of UTTs on TCs is here attributed to their disparate distance criteria (5 degrees for TCs and 10 degrees for UTTs). TCs are more frequent to the west of Sub7 while easterly UTTs prevail as shown in Table 1. Since, in a compound event, UTT centers are usually far from the TC centers, the TC precipitation is largely unaffected by UTTs. However, when we decrease the distance criterion to 5 degrees for UTTs, the TC-UTT curve indeed shows lower probabilities for high precipitation rates in Figure 21, indicating that UTTs tend to weaken TC precipitation. A further examination of the composites shows UTTs hinder the eastward moisture transportation by TCs, which decreases the local water content in Sub7. This is in accord with previous research showing that UTTs can decrease TC activity (Zhang et al., 2016, 2017; Z. Wang et al., 2020).

4.5.3 Fronts and mid-tropospheric lows

Mid-tropospheric lows and fronts are selected as major drivers of EPEs for Sub4 and Sub5 since they are frequent in these inland areas. As has been demonstrated in section 4.3, mid-tropospheric lows occur simultaneously with strong frontal systems. Consequently, we focus here on the precipitation caused by fronts and mid-tropospheric lows, as opposed to precipitation induced solely by fronts. Comparing the PDFs, fronts are more likely to produce heavy precipitation when mid-tropospheric lows are concurrent for both Sub4 and Sub5 as depicted in Figure 21. Similar meteorology patterns are observed as in Figure 17, suggesting that mid-tropospheric lows are associated with larger anomalies in both water content and vertical velocity fields.

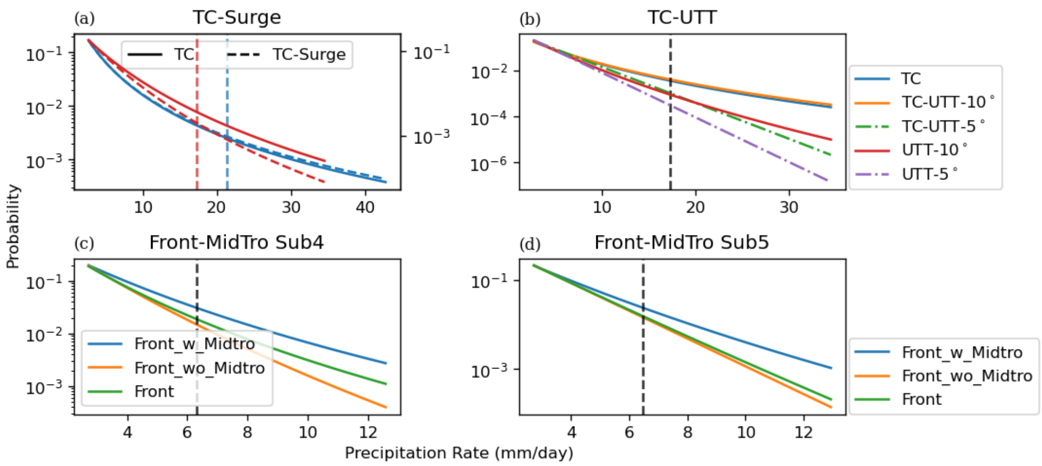

Figure 21. Double-feature PDF curves: (a) TC and GOC surge in Sub1 (blue) and Sub7 (red); (b) TC and UTT with different distance thresholds in Sub7; (c) front and mid-tropospheric lows in Sub4 and (d) Sub5. Dashed vertical lines represent the EPE threshold.

4.5.4 UTTs and MCSs

As shown in Figure 8, eastward-UTTs and westward-UTTs show distinct precipitation anomalies. With this in mind, we consider a decomposition of UTTs by their propagation directions. Figure 22 depicts the UTT-precipitation PDF curves with and without MCSs. For westward UTTs, presence of a MCS will increase the precipitation rate, as the orange curves (UTTwMCS) are always above the blue curves (UTTwoMCS) in the high precipitation rate regimes. To the contrary, precipitation induced by eastward-UTTs tends to be depressed when MCSs are co-occurring, as the UTTwMCS curves are under the UTTwoMCS curves for Sub6 and Sub7. This indicates that westward-UTTs enhance precipitation in MCSs by increasing convective activity, as suggested in the case studies in Finch and Johnson (2010b); Newman and Johnson (2012), although the enhancement is small. Additionally, these case studies have also demonstrated that convective systems are more common in the Sierra Madre. This relatively static location of MCS systems is not always at the same distance to the UTT centers during their westward propagation. This mismatch could potentially result in the fragments of precipitation anomaly composites for westward-UTTs observed in Figure 8.

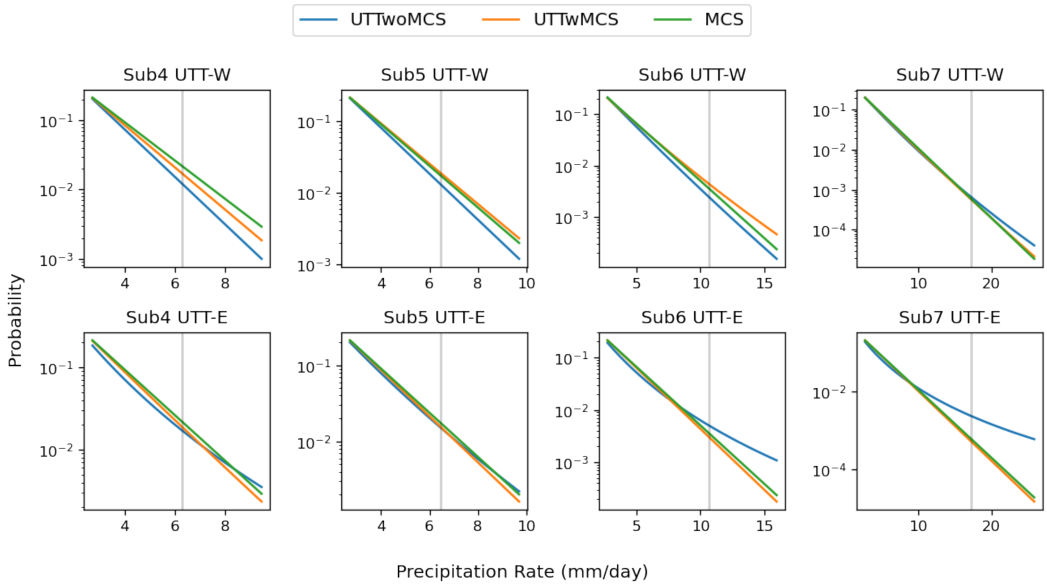

Figure 22. UTT and MCS precipitation probability density functions and their interactions. Top row is for westward-UTTs and bottom for eastward-UTTs. UTTwoMCS stands for precipitation induced solely by UTTs, and UTTwMCS represents the precipitation caused by both UTT and MCS.

5 Conclusions

This work investigates the meteorological drivers for EPEs in the NAM region from 1979 to 2018. We first delineate the NAM domain and its subregions from the CPC precipitation dataset, rather than using individual states or latitude-longitude bounded areas. Since the SOM-based identification method emphasizes the extreme precipitation characteristics and doesn't rely on topographical features or state borders, it is better suited to regional precipitation studies. Given the heterogeneous topographical characteristics and precipitation distributions in the NAM region, the subregion delineation is still necessary to understand the precipitation drivers.

Candidate meteorological features selected to investigate as drivers of EPEs include TCs, UTTs, GOC moisture surges, fronts, mid-tropospheric lows and MCSs. This selection appears sufficient to capture all EPE drivers, as essentially all EPEs fall into at least one of these categories; for the singular unclassified EPE after 2003, the PV200 anomalies are quite weak, and its precipitation rate is close to our EPE threshold. This connection suggests a potential quantitative link between precipitation and meteorological conditions. Unsurprisingly, different subregions have different dominant drivers, and most EPEs are associated with more than one driver. Given the larger EPE precipitation fraction associated solely to them, GOC surges, MCSs and fronts tend to be the most important. This finding highlights the importance of developing MCS and front datasets for the NAM region prior to 2003. The attribution of all EPEs to feature drivers does not indicate these drivers are sufficient conditions for EPE occurrence. Indeed, the probability of an EPEs given the presence of these drivers is generally less than 30%. Additionally, the driver with the highest extreme precipitation probability for each subregion is not the driver that produces the most extreme precipitation, reflecting variations in the frequency of each feature driver.

EPE composites indicate that extreme precipitation events are associated with both high local water vapor content (Q850, TCWV) and upward lifting (Ω500, CAPE). Further examination shows significantly positive IVT-B anomalies for inland areas, indicating the important role of onshore moisture transport in addition to IVT-A. Close associations are found between TCs and GOC surges, and between mid-tropospheric lows and fronts. For UTT-EPEs, the propagation direction of the upper-level disturbance plays a major role in the subsequent precipitation anomalies. Because of the direction in environmental winds, there are more westerly disturbances for northern subregions (e.g., Sub3) whereas easterlies are more common for southern subregions (e.g., Sub6 and Sub7). Both types of UTTs tend to suppress precipitation to the north of the feature and enhance it to the south, although the enhancement is weak for westward propagating UTTs. Our double driver analysis suggests co-occurring UTTs tend to suppress TC precipitation, but may be enhanced by MCS (although these results are sensitive to subregion).

We are primarily interested in the co-occurrence of atmospheric drivers with EPEs, which does not necessarily indicate causality. In terms of future research, a causal inference analysis could be conducted to better examine the conditions necessary for a feature to produce an EPE. Additionally, given the modest PV200 anomalies for the unclassified EPE with a lower precipitation rate, we see chances to incorporate quantitative analysis between atmospheric drivers and precipitation rates. Some quantitative analysis, like Sukhdeo et al. (2022), could be used to quantify the predictability. Overall, the work presented here aims to better quantify the relative importance of meteorological drivers to EPEs in different monsoonal subregions. Future work will seek to apply a similar analysis to other global regions.

Acknowledgments

ERA5 data can be accessed at `https://cds.climate.copernicus.eu`. The CPC global precipitation dataset is available at `https://psl.noaa.gov/data/gridded/data.cpc.globalprecip.html`. Our NAM domain shapefiles and GOC moisture surge records can be accessed at Duan et al. (2022). This material is based upon work supported by the U.S. Department of Energy, Office of Science, Office of Biological and Environmental Research, Climate and Environmental Sciences Division, Regional and Global Model Analysis Program, under Award DE-SC0019367 and DE-SC0016605. Computational resources are from the National Energy Research Scientific Computing Center (NERSC), which is a DOE Office of Science User Facility and the Tempest cluster at UC Davis. Special thanks to Dr. Matthew Igel for helpful discussions.

References

Acero, F. J., García, J. A., & Gallego, M. C. (2011). Peaks-over-threshold study of trends in extreme rainfall over the iberian peninsula. *Journal of Climate*, *24*(4), 1089–1105.

Agel, L., Barlow, M., Feldstein, S. B., & Gutowski, W. J. (2018). Identification of large-scale meteorological patterns associated with extreme precipitation in the us northeast. *Climate dynamics*, *50*(5-6), 1819–1839.

Alaya, B., Zwiers, F., & Zhang, X. (2020). An evaluation of block-maximum based estimation of very long return period precipitation extremes with a large ensemble climate simulation. *Journal of Climate*.

Anagnostopoulou, C., & Tolika, K. (2012). Extreme precipitation in europe: statistical threshold selection based on climatological criteria. *Theoretical and Applied Climatology*, *107*(3), 479–489.

Barlow, M., Gutowski, W. J., Gyakum, J. R., Katz, R. W., Lim, Y.-K., Schumacher, R. S., … others (2019). North american extreme precipitation events and related large-scale meteorological patterns: a review of statistical methods, dynamics, modeling, and trends. *Climate Dynamics*, *53*(11), 6835–6875.

Biard, J. C. (2019, April). *National Weather Service Coded Surface Bulletins, 2003- (netCDF format).* Zenodo. Retrieved from https://doi.org/10.5281/zenodo.2651361 doi: 10.5281/zenodo.2651361

Biard, J. C., & Kunkel, K. E. (2019). Automated detection of weather fronts using a deep learning neural network. *Advances in Statistical Climatology, Meteorology and Oceanography*, *5*(2), 147–160.

Bieda III, S. W., Castro, C. L., Mullen, S. L., Comrie, A. C., & Pytlak, E. (2009). The relationship of transient upper-level troughs to variability of the north american monsoon system. *Journal of Climate*, *22*(15), 4213–4227.

Boos, W., & Pascale, S. (2021). Mechanical forcing of the north american monsoon by orography.

Bordoni, S., & Stevens, B. (2006). Principal component analysis of the summertime winds over the gulf of california: A gulf surge index. *Monthly weather review*, *134*(11), 3395–3414.

Catto, J., Jakob, C., Berry, G., & Nicholls, N. (2012). Relating global precipitation to atmospheric fronts. *Geophysical Research Letters*, *39*(10).

Chen, G. T.-J., & Chou, L.-F. (1994). An investigation of cold vortices in the upper troposphere over the western north pacific during the warm season. *Monthly weather review*, *122*(7), 1436–1448.

Cook, B. I., & Seager, R. (2013). The response of the north american monsoon to increased greenhouse gas forcing. *Journal of Geophysical Research: Atmospheres*, *118*(4), 1690–1699.

Dargahi-Noubary, G. (1989). On tail estimation: an improved method. *Mathematical Geology*, *21*(8), 829–842.

de Carvalho, L. M. V., & Jones, C. (Eds.). (2016). *The monsoons and climate change*. Springer International Publishing. Retrieved from https://doi.org/10.1007/978-3-319-21650-8 doi: 10.1007/978-3-319-21650-8

Díaz, S., Salinas-Zavala, C., & Hernández-Vázquez, S. (2008). Variability of rainfall from tropical cyclones in northwestern méxico and its relation to soi and pdo. *Atmósfera*, *21*(2), 213–223.

Dominguez, C., & Magaña, V. (2018). The role of tropical cyclones in precipitation over the tropical and subtropical north america. *Frontiers in Earth Science*, *6*, 19.

Dominguez, F., Miguez-Macho, G., & Hu, H. (2016). Wrf with water vapor tracers: A study of moisture sources for the north american monsoon. *Journal of Hydrometeorology*, *17*(7), 1915–1927.

Douglas, A. V., & Englehart, P. J. (2007). A climatological perspective of transient synoptic features during name 2004. *Journal of climate*, *20*(9), 1947–1954.

Duan, S., Ullrich, P., & Boos, W. (2022, November). *North American Monsoon Domain and Gulf of California Moisture Surges.* Zenodo. Retrieved from https://doi.org/10.5281/zenodo.7314498 doi: 10.5281/zenodo.7314498

Englehart, P. J., & Douglas, A. V. (2001). The role of eastern north pacific tropical storms in the rainfall climatology of western mexico. *International Journal of Climatology: A Journal of the Royal Meteorological Society*, *21*(11), 1357–1370.

Feng, Z., Leung, L. R., Liu, N., Wang, J., Houze Jr, R. A., Li, J., … Guo, J. (2021).

A global high-resolution mesoscale convective system database using satellite-derived cloud tops, surface precipitation, and tracking. *Journal of Geophysical Research: Atmospheres*, *126*(8), e2020JD034202.

Finch, Z. O., & Johnson, R. H. (2010a). Observational analysis of an upper-level inverted trough during the 2004 north american monsoon experiment. *Monthly weather review*, *138*(9), 3540–3555.

Finch, Z. O., & Johnson, R. H. (2010b). Observational analysis of an upper-level inverted trough during the 2004 north american monsoon experiment. *Monthly Weather Review*, *138*(9), 3540–3555. doi: 10.1175/2010MWR3369.1

Fuentes-Franco, R., Koenigk, T., Docquier, D., Graef, F., & Wyser, K. (2022). Exploring the influence of the north pacific rossby wave sources on the variability of summer atmospheric circulation and precipitation over the northern hemisphere. *Climate Dynamics*, 1–15.

Geen, R., Bordoni, S., Battisti, D. S., & Hui, K. (2020). Monsoons, itczs, and the concept of the global monsoon. *Reviews of Geophysics*, *58*(4), e2020RG000700.

Goswami, B. N., Krishnamurthy, V., & Annmalai, H. (1999). A broad-scale circulation index for the interannual variability of the indian summer monsoon. *Quarterly Journal of the Royal Meteorological Society*, *125*(554), 611–633.

Hersbach, H., Bell, B., Berrisford, P., Hirahara, S., Horányi, A., Muñoz-Sabater, J., . . . others (2020). The era5 global reanalysis. *Quarterly Journal of the Royal Meteorological Society*, *146*(730), 1999–2049.

Hewson, T. D. (1998). Objective fronts. *Meteorological Applications*, *5*(1), 37–65.

Higgins, R., Yao, Y., & Wang, X. (1997). Influence of the north american monsoon system on the us summer precipitation regime. *Journal of climate*, *10*(10), 2600–2622.

Higgins, W., Ahijevych, D., Amador, J., Barros, A., Berbery, E. H., Caetano, E., . . . others (2006). The name 2004 field campaign and modeling strategy. *Bulletin of the American Meteorological Society*, *87*(1), 79–94.

Houssos, E., Lolis, C., & Bartzokas, A. (2008). Atmospheric circulation patterns associated with extreme precipitation amounts in greece. *Advances in Geosciences*, *17*, 5–11.

Hung, C.-W., & Yanai, M. (2004). Factors contributing to the onset of the australian summer monsoon. *Quarterly Journal of the Royal Meteorological Society: A journal of the atmospheric sciences, applied meteorology and physical oceanography*, *130*(597), 739–758.

Igel, M. R., Ullrich, P. A., & Boos, W. R. (2021). Upper-tropospheric troughs and north american monsoon rainfall in a long-term track dataset. *Journal of Geophysical Research: Atmospheres*, e2021JD034541.

Jiang, H., & Zipser, E. J. (2010). Contribution of tropical cyclones to the global precipitation from eight seasons of trmm data: Regional, seasonal, and interannual variations. *Journal of climate*, *23*(6), 1526–1543.

Kelley, W. E., & Mock, D. R. (1982). A diagnostic study of upper tropospheric cold lows over the western north pacific. *Monthly Weather Review*, *110*(6), 471–480.

Klotzbach, P. J., Wood, K. M., Schreck III, C. J., Bowen, S. G., Patricola, C. M., & Bell, M. M. (2022). Trends in global tropical cyclone activity: 1990–2021. *Geophysical Research Letters*, *49*(6), e2021GL095774.

Knapp, K. R., Diamond, H. J., Kossin, J. P., Kruk, M. C., & Schreck, C. J. (2018). *International best track archive for climate stewardship (ibtracs) project, version 4.* NOAA National Centers for Environmental Information. Retrieved from `https://data.nodc.noaa.gov/cgi-bin/iso?id=gov.noaa.ncdc:C01552` doi: 10.25921/82TY-9E16

Knapp, K. R., Kruk, M. C., Levinson, D. H., Diamond, H. J., & Neumann, C. J. (2010). The international best track archive for climate stewardship (ibtracs) unifying tropical cyclone data. *Bulletin of the American Meteorological Society*, *91*(3), 363–376.

Kohonen, T., & Honkela, T. (2007). Kohonen network. *Scholarpedia*, *2*(1), 1568.

Kunkel, K. E., Easterling, D. R., Kristovich, D. A., Gleason, B., Stoecker, L., & Smith, R. (2012). Meteorological causes of the secular variations in observed extreme precipitation events for the conterminous united states. *Journal of Hydrometeorology*, *13*(3), 1131–1141.

Lee, J.-Y., & Wang, B. (2014). Future change of global monsoon in the cmip5. *Climate Dynamics*, *42*(1-2), 101–119.

Liu, F., Chai, J., Wang, B., Liu, J., Zhang, X., & Wang, Z. (2016). Global monsoon precipitation responses to large volcanic eruptions. *Scientific reports*, *6*(1), 1–11.

Martinez-Villalobos, C., & Neelin, J. D. (2019). Why do precipitation intensities tend to follow gamma distributions? *Journal of the Atmospheric Sciences*, *76*(11), 3611–3631.

Mejia, J. F., Douglas, M. W., & Lamb, P. J. (2016). Observational investigation of relationships between moisture surges and mesoscale-to large-scale convection during the north american monsoon. *International Journal of Climatology*, *36*(6), 2555–2569.

Mohtadi, M., Prange, M., & Steinke, S. (2016). Palaeoclimatic insights into forcing and response of monsoon rainfall. *Nature*, *533*(7602), 191–199.

Moore, B. J., Keyser, D., & Bosart, L. F. (2019). Linkages between extreme precipitation events in the central and eastern united states and rossby wave breaking. *Monthly Weather Review*, *147*(9), 3327–3349.

Murakami, H., Delworth, T. L., Cooke, W. F., Zhao, M., Xiang, B., & Hsu, P.-C. (2020). Detected climatic change in global distribution of tropical cyclones. *Proceedings of the National Academy of Sciences*, *117*(20), 10706–10714.

Myhre, G., Alterskjær, K., Stjern, C. W., Hodnebrog, Ø., Marelle, L., Samset, B. H., ... others (2019). Frequency of extreme precipitation increases extensively with event rareness under global warming. *Scientific reports*, *9*(1), 1–10.

Newman, A., & Johnson, R. H. (2012). Mechanisms for precipitation enhancement in a North American Monsoon upper-tropospheric trough. *Journal of the Atmospheric Sciences*, *69*(6), 1775–1792.

Papin, P. P., Bosart, L. F., & Torn, R. D. (2020). A feature-based approach to classifying summertime potential vorticity streamers linked to rossby wave breaking in the north atlantic basin. *Journal of Climate*, *33*(14), 5953–5969.

Parfitt, R., Czaja, A., & Seo, H. (2017). A simple diagnostic for the detection of atmospheric fronts. *Geophysical Research Letters*, *44*(9), 4351–4358.

Pazos, M., & Mendoza, B. (2013). Landfalling tropical cyclones along the eastern pacific coast between the sixteenth and twentieth centuries. *Journal of climate*, *26*(12), 4219–4230.

Perneger, T. V. (1998). What's wrong with bonferroni adjustments. *Bmj*, *316*(7139), 1236–1238.

Ramage, C. S. (1971). *Monsoon meteorology* (Tech. Rep.).

Ryoo, J.-M., Kaspi, Y., Waugh, D. W., Kiladis, G. N., Waliser, D. E., Fetzer, E. J., & Kim, J. (2013). Impact of rossby wave breaking on us west coast winter precipitation during enso events. *Journal of Climate*, *26*(17), 6360–6382.

Sierks, M. D., Kalansky, J., Cannon, F., & Ralph, F. (2020). Characteristics, origins, and impacts of summertime extreme precipitation in the lake mead watershed. *Journal of Climate*, *33*(7), 2663–2680.

Stidd, C. (1953). Cube-root-normal precipitation distributions. *Eos, Transactions American Geophysical Union*, *34*(1), 31–35.

Sukhdeo, R., Ullrich, P. A., & Grotjahn, R. (2022). Assessing the large-scale drivers of precipitation in the northeastern united states via linear orthogonal decomposition. *Climate Dynamics*, 1–25.

Swenson, L. M., & Grotjahn, R. (2019). Using self-organizing maps to identify coherent conus precipitation regions. *Journal of Climate*, *32*(22), 7747–7761.
Turrent, C., & Cavazos, T. (2009). Role of the land-sea thermal contrast in the interannual modulation of the north american monsoon. *Geophysical Research Letters*, *36*(2).
Ullrich, P. A., Zarzycki, C. M., McClenny, E. E., Pinheiro, M. C., Stansfield, A. M., & Reed, K. A. (2021). Tempestextremes v2. 1: a community framework for feature detection, tracking and analysis in large datasets. *Geoscientific Model Development Discussions*, 1–37.
Varuolo-Clarke, A. M., Reed, K. A., & Medeiros, B. (2019). Characterizing the north american monsoon in the community atmosphere model: Sensitivity to resolution and topography. *Journal of Climate*, *32*(23), 8355–8372.
Vera, C., Higgins, W., Amador, J., Ambrizzi, T., Garreaud, R., Gochis, D., ... others (2006). Toward a unified view of the american monsoon systems. *Journal of climate*, *19*(20), 4977–5000.
Wang, B., & Fan, Z. (1999). Choice of south asian summer monsoon indices. *Bulletin of the American Meteorological Society*, *80*(4), 629–638.
Wang, B., Li, J., Cane, M. A., Liu, J., Webster, P. J., Xiang, B., ... Ha, K.-J. (2018). Toward predicting changes in the land monsoon rainfall a decade in advance. *Journal of Climate*, *31*(7), 2699–2714.
Wang, F., Shao, W., Yu, H., Kan, G., He, X., Zhang, D., ... Wang, G. (2020). Re-evaluation of the power of the mann-kendall test for detecting monotonic trends in hydrometeorological time series. *Frontiers in Earth Science*, 14.
Wang, Z., Zhang, G., Dunkerton, T. J., & Jin, F.-F. (2020). Summertime stationary waves integrate tropical and extratropical impacts on tropical cyclone activity. *Proceedings of the National Academy of Sciences*, *117*(37), 22720–22726.
Watterson, I., & Dix, M. (2003). Simulated changes due to global warming in daily precipitation means and extremes and their interpretation using the gamma distribution. *Journal of Geophysical Research: Atmospheres*, *108*(D13).
Webster, P. J., & Yang, S. (1992). Monsoon and enso: Selectively interactive systems. *Quarterly Journal of the Royal Meteorological Society*, *118*(507), 877–926.
Wibig, J. (1999). Precipitation in europe in relation to circulation patterns at the 500 hpa level. *International Journal of Climatology: A Journal of the Royal Meteorological Society*, *19*(3), 253–269.
Xie, P., Chen, M., & Shi, W. (2010). Cpc unified gauge-based analysis of global daily precipitation. In *Preprints, 24th conf. on hydrology, atlanta, ga, amer. meteor. soc* (Vol. 2).
Zavadoff, B. L., & Kirtman, B. P. (2019). North atlantic summertime anticyclonic rossby wave breaking: Climatology, impacts, and connections to the pacific decadal oscillation. *Journal of Climate*, *32*(2), 485–500.
Zhang, G., Wang, Z., Dunkerton, T. J., Peng, M. S., & Magnusdottir, G. (2016). Extratropical impacts on atlantic tropical cyclone activity. *Journal of the Atmospheric Sciences*, *73*(3), 1401–1418.
Zhang, G., Wang, Z., Peng, M. S., & Magnusdottir, G. (2017). Characteristics and impacts of extratropical rossby wave breaking during the atlantic hurricane season. *Journal of Climate*, *30*(7), 2363–2379.
Zhao, M. (2022). A study of ar-, ts-, and mcs-associated precipitation and extreme precipitation in present and warmer climates. *Journal of Climate*, *35*(2), 479–497.